

The Arctic Ocean double estuary: quantification and forcing mechanisms

Article

Published Version

Creative Commons: Attribution 4.0 (CC-BY)

Open Access

Brown, N. J. ORCID: https://orcid.org/0000-0001-6222-8850, Naveira Garabato, A. C. ORCID: https://orcid.org/0000-0001-6071-605X, Bacon, S. ORCID: https://orcid.org/0000-0002-2471-9373, Aksenov, Y., Tsubouchi, T. ORCID: https://orcid.org/0000-0001-6774-8847, Green, M. ORCID: https://orcid.org/0000-0001-5090-1040, Lincoln, B. ORCID: https://orcid.org/0000-0002-0314-3109, Rippeth, T. ORCID: https://orcid.org/0000-0002-9286-0176 and Feltham, D. L. ORCID: https://orcid.org/0000-0003-2289-014X (2025) The Arctic Ocean double estuary: quantification and forcing mechanisms. AGU Advances, 6 (6). e2024AV001529. ISSN 2576-604X doi: 10.1029/2024av001529 Available at https://centaur.reading.ac.uk/127019/

It is advisable to refer to the publisher's version if you intend to cite from the work. See <u>Guidance on citing</u>.

To link to this article DOI: http://dx.doi.org/10.1029/2024av001529

Publisher: American Geophysical Union (AGU)

All outputs in CentAUR are protected by Intellectual Property Rights law,



including copyright law. Copyright and IPR is retained by the creators or other copyright holders. Terms and conditions for use of this material are defined in the <u>End User Agreement</u>.

www.reading.ac.uk/centaur

CentAUR

Central Archive at the University of Reading

Reading's research outputs online



AGU Advances



RESEARCH ARTICLE

10.1029/2024AV001529

Peer Review The peer review history for this article is available as a PDF in the Supporting Information.

Key Points:

- The Arctic Ocean double estuary circulation is assessed from measurements at the four oceanic gateways to the region
- Atlantic Water lighter than $\sigma_0 = 27.75 \text{ kg m}^{-3}$ upwells into less dense waters at a rate of 1.8 Sv (1 Sv = $10^6 \text{ m}^3 \text{ s}^{-1}$), driven by tidally-induced turbulent mixing
- Denser Atlantic Water downwells into denser classes at a rate of 1.5 Sv, driven by surface heat loss in the Barents Sea

Supporting Information:

Supporting Information may be found in the online version of this article.

Correspondence to:

A. C. Naveira Garabato acng@soton.ac.uk

Citation

Brown, N. J., Naveira Garabato, A. C., Bacon, S., Aksenov, Y., Tsubouchi, T., Green, M., et al. (2025). The Arctic Ocean double estuary: Quantification and forcing mechanisms. *AGU Advances*, 6, e2024AV001529. https://doi.org/10.1029/2024AV001529

Received 1 OCT 2024 Accepted 12 OCT 2025

Author Contributions:

Sheldon Bacon
Formal analysis: Nikki J. Brown
Funding acquisition: Alberto C. Naveira
Garabato, Sheldon Bacon
Investigation: Nikki J. Brown, Alberto
C. Naveira Garabato, Sheldon Bacon
Methodology: Nikki J. Brown, Alberto
C. Naveira Garabato, Sheldon Bacon,
Takamasa Tsubouchi, Mattias Green
Project administration: Sheldon Bacon
Software: Nikki J. Brown

Conceptualization: Nikki J. Brown,

Alberto C. Naveira Garabato,

© 2025. The Author(s).

This is an open access article under the terms of the Creative Commons

Attribution License, which permits use, distribution and reproduction in any medium, provided the original work is properly cited.

The Arctic Ocean Double Estuary: Quantification and Forcing Mechanisms

Nikki J. Brown^{1,2}, Alberto C. Naveira Garabato¹, Sheldon Bacon^{1,3,4}, Yevgeny Aksenov³, Takamasa Tsubouchi⁵, Mattias Green⁴, Ben Lincoln⁴, Tom Rippeth⁴, and Daniel L. Feltham⁶

¹University of Southampton, Southampton, UK, ²Swedish Meteorological and Hydrological Institute, Norrköping, Sweden, ³National Oceanography Centre, Southampton, UK, ⁴Bangor University, Bangor, UK, ⁵Japan Meteorological Agency, Tokyo, Japan, ⁶University of Reading, Reading, UK

Abstract The Arctic Ocean double estuary is a "three-legged" overturning system in which inflowing waters are converted into both lighter and denser waters before being exported equatorwards. As the northern terminus of the Atlantic Meridional Overturning Circulation (MOC), it thus both affects, and is affected by, the Atlantic MOC. Here we quantify the magnitudes of the two overturning cells in density space, and then decompose the water mass transformation rates into net pan-Arctic contributions from surface forcing and diapycnal mixing. We use a high-resolution, quasi-synoptic ice and ocean hydrographic data set spanning the four main Arctic Ocean gateways—Fram, Davis and Bering Straits, and the Barents Sea Opening. Two surface flux reanalyses and a hydrographic climatology are used to generate estimates of surface water mass transformation rates by density class. A box model then determines the profiles of turbulent mixing transformation rates, and associated turbulent diffusivities. We show that turbulent mixing and surface forcing drive transformations of similar magnitudes, while mixing dominates in the upper cell and surface fluxes in the lower cell. Consideration of uncertainties and timescales leads to the tentative suggestion that our results might be representative of recent decades. We discuss the possible significance of tides and sea ice brine rejection as energy sources driving turbulent mixing. Finally, we speculate as to whether water mass transformation rates may change in future as ocean heat transport into the Arctic increases. As sea ice declines and the efficiency of atmosphere-to-ocean momentum transfer increases, the Arctic Ocean is expected to "spin up," causing more intense turbulent mixing, with uncertain consequences.

Plain Language Summary The Arctic Ocean has been covered by sea ice year-round for much of the past, inhibiting the impact of wind on the ocean, with the consequence that Arctic Ocean currents are generally slow and turbulent mixing weak. However, recent decades have seen accelerated warming of the Arctic atmosphere and a reduction in sea ice cover, and more recently, an expansion of warm Atlantic waters in the region is beginning to be observed. Motivated by these changes, here we use observations from the Arctic Ocean's boundaries to investigate its vertical circulation, in which inflowing Atlantic waters are transformed into both lighter (upwelling) and denser (downwelling) waters. We find that the Arctic Ocean's upwelling limb is mainly driven by turbulent mixing, while the downwelling limb is primarily forced by loss of oceanic heat to the atmosphere in the ice-free Barents Sea. We build on these new insights to discuss how the vertical circulation of the Arctic Ocean may change in future as sea ice retreats and the wind's influence on the ocean increases, leading to speeding up of Arctic currents and more intense turbulent mixing.

1. Introduction

Our motivation for this study is the idea of the Arctic Ocean as a double estuary. Inflowing waters, mainly of Atlantic origin, enter the Arctic Ocean via Fram Strait and the Barents Sea Opening (Figure 1). These waters are converted both to lighter waters (the positive estuary), mainly by freshwater addition, and to denser waters (the negative estuary), mainly via heat loss. The double estuary is important outside the Arctic because both lighter and denser waters are ultimately exported back into the northern North Atlantic. The denser component then forms part of the deep, south-going limb of the Atlantic Meridional Overturning Circulation (MOC), while the lighter component becomes a major part of the North Atlantic Subpolar Gyre's western boundary current system. The lighter component can then increase the Subpolar Gyre's stratification and decrease its rate of dense water formation, in turn affecting the MOC itself. However, changes in the Atlantic MOC can also affect the double

BROWN ET AL. 1 of 22

2576694x, 2025, 6, Downloaded from https://agupubs.onlinelibrary.wiley.com/doi/10.1029/2024AV001529 by NICE, National Institute for Health and Care Excellence, Wiley Online Library on [18/1/2025]. See the Terms

Supervision: Alberto C. Naveira Garabato, Sheldon Bacon Validation: Nikki J. Brown Writing – original draft: Sheldon Bacon Writing – review & editing: Alberto C. Naveira Garabato, Yevgeny Aksenov, Takamasa Tsubouchi, Mattias Green, Ben Lincoln, Tom Rippeth, Daniel L. Feltham

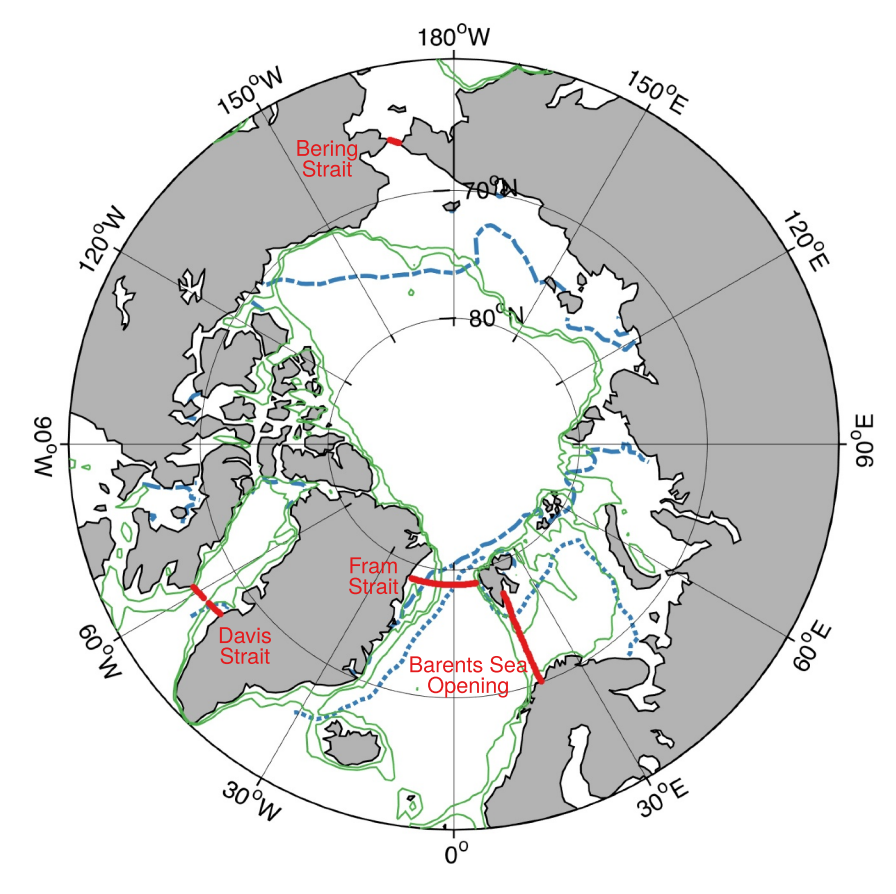


Figure 1. Control volume domain showing the locations of the four ocean gateways (red), 200 and 500 m depth contours (green), and mean sea ice extent defined as the limit of 15% ice cover, from ERA-Interim for September 2004 and April 2005 (dashed and dotted blue lines respectively).

estuary: for instance, changes in the volume and/or the temperature of the north-going Atlantic waters will change the ocean heat supply to the Arctic. Weijer et al. (2022) provide a recent review of interactions between the Arctic Ocean and the Atlantic MOC.

Stigebrandt (1981) introduced the idea that the Arctic Ocean may possess properties of both positive and negative estuaries, in considering the processes influencing the thickness and salinity of the Arctic Ocean upper layer (effectively the upper 200 m, i.e. the halocline), and found a relationship between sea ice thickness and freshwater supply. E. Carmack and Wassmann (2006) extended this idea to describe the Arctic Ocean double estuary coupled to the meridional thermohaline circulation (i.e., the MOC). In so doing, they provided a schematic description of the progress of Atlantic waters through the Nordic Seas and into the Arctic Ocean, and noted the cooling and freshening that are the main contributors to the formation of the denser and lighter waters (respectively). E. C. Carmack (2007) then used the double estuary description as part of his assessment of the geographical separation of stratification (predominantly) by temperature from that by salinity in the World Ocean.

Increasingly complex representations of the double estuary were subsequently developed. Rudels (2010) applied a theoretical approach constrained by measurements to describe (in a narrative sense, and amongst other things) the oceanographic conditions that lead to the separation of lighter and denser estuarine loops. Eldevik and Nilsen (2013) applied an approach based on measurements and budgets to constrain the strength and structure of the double estuary. They found that the strength of the Atlantic inflow is largely insensitive to anomalous freshwater input and mainly reflects changes in Nordic Seas and Arctic Ocean heat loss. Lambert et al. (2016) used a three-box model to represent the double estuary in terms of inflows and the two varieties (lighter and denser) of outflows. They found that the net inflow into the double estuary is more sensitive to a change in the distribution of freshwater than to a change in the total freshwater input. Haine (2021) applied a conceptual model to both polar oceans. For the Arctic, he found that the negative estuarine circulation (the dense water loop) is probably robust,

BROWN ET AL. 2 of 22

onlinelibrary.wiley.com/doi/10.1029/2024AV001529 by NICE,

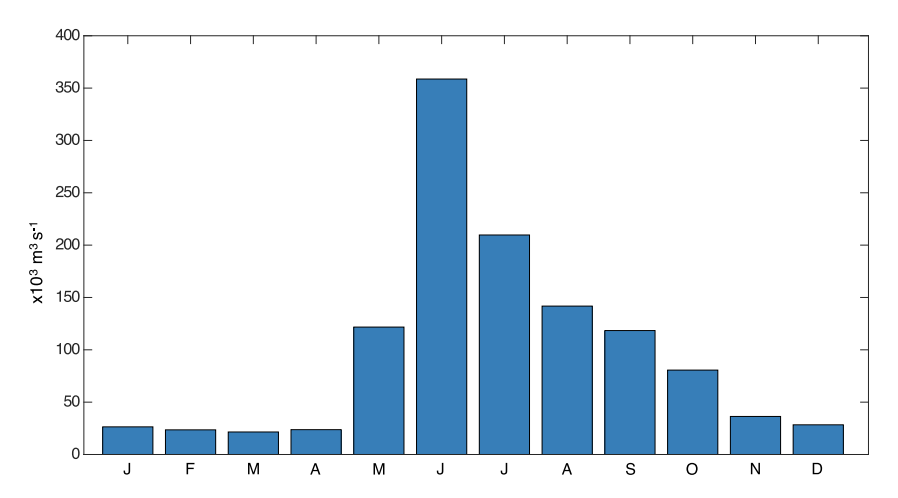


Figure 2. Total (gauged plus ungauged) Arctic river runoff volume flux from the Arctic Ocean Model Intercomparison Project data set by calendar month.

but that the positive circulation (the lighter loop) may be vulnerable to collapse via a "heat crisis," entailed either by increasing oceanic (Atlantic water) heat flux, increasing surface freshwater flux, and/or decreasing heat loss from ocean to atmosphere. While these conceptual studies explored the forcing and sensitivities of the Arctic Ocean double estuary, Rudels and Carmack (2022) observed that these "models ignore, as do most conceptual models ... the inflow over the Barents Sea. The Barents Sea inflow is largely barotropic and mainly forced by wind and sea level slope and cannot easily be incorporated in the baroclinic description used for double estuary exchanges through Fram Strait." The importance of the Barents Sea is emphasized by the coupled model study of Oldenburg et al. (2024), who found future Arctic warming to be driven primarily by increased ocean heat transport through the Barents Sea Opening.

Meanwhile, in an attempt to approach a more realistic description of the water mass transformations inherent in the Arctic Ocean double estuary, Pemberton et al. (2015) used a temperature/salinity framework applied to a coarse-resolution (1°) general circulation model to diagnose transformation rates across isothermal and isohaline surfaces. They found that water mass transformation in "the temperature direction" is mainly accomplished by surface heat fluxes, while the surface freshwater flux only plays a small role in the transformation of water toward lower salinities, which is mainly driven by a downgradient mixing of salt in the interior ocean. Their study is compromised, however, by "model deficiencies," which include the coarse resolution, the unrealistically-weak inflows and outflows through Fram Strait, and the model's lack of a halocline.

The first attempt to quantify the Arctic Ocean double estuary from measurements is seen in Tsubouchi et al. (2012; T2012 hereafter). They applied an inverse model to quasi-synoptic ice and ocean measurements across the four Arctic Ocean gateways of Fram, Davis and Bering Straits and the Barents Sea Opening (Figure 1). They diagnosed volume exchanges between density layers (their Figure 11) but their uncertainties precluded any definitive statements at the time. However, the subsequent analysis of Tsubouchi et al. (2024) employed a much larger quantity of measurements in the same locations, leading to a statistically-significant quantification of the double estuary in terms of volume exchanges between density layers. Results from both papers will be described in detail below. Between these two papers, Tsubouchi et al. (2021) applied the same inverse method to the Nordic Seas.

Turning to turbulent (vertical/diapycnal) mixing in the Arctic Ocean, a notable early review is provided by Padman (1995). He divided Arctic Ocean mixing processes into two categories—those resulting from contact with an ocean boundary (i.e., the atmosphere, the base of the sea ice, or the sea bed), and those occurring in the pycnocline (away from the direct influence of boundaries). His Figure 2 summarizes significant mixing processes, and his Figure 9 is a flow chart that relates forcings to an array of physical ice and ocean phenomena. Winds and tides are noted as sources of mechanical energy to drive mixing, while thermal energy can also drive mixing via the rejection of dense brines consequent on the freezing-out of sea ice. In the course of reviewing the state of knowledge and understanding of the array of relevant physical processes, he also noted the high spatial (vertical and horizontal) and temporal (seasonal) variability allied to these processes. In more recent years, novel

BROWN ET AL. 3 of 22



measurements and improved numerical models have advanced understanding of the energy pathways leading to mixing, as reviewed by Lenn et al. (2022) and Ripperth and Fine (2022). New physical pathways of energy that lead to turbulent mixing have been identified, including via the development of unsteady lee waves (Rippeth et al., 2017).

However, perhaps the most important development in this context has been the appreciation of the significance of the changing Arctic for the Arctic Ocean. Quoting Lenn et al. (2022), "we observe notable changes in sea-ice volume, ocean heat and fresh water content, the strength and distribution of vertical stratification and the distribution of the warm [Atlantic water] ... Overall, these changes will affect wind forcing, near-inertial wave radiation, baroclinic tide generation and radiation, double-diffusive processes, and the ultimate dissipation and vertical mixing in the water column."

For the Arctic Ocean double estuary, the main development has been its quantification by T2012 and Tsubouchi et al. (2024). Microstructure measurements have been made in many locations, as exemplified by the multi-year, upper-ocean survey in mainly ice-free waters of pan-Arctic turbulent mixing rates by Rippeth et al. (2015). However, there exists no pan-Arctic quantification of net turbulent mixing rates, nor of their role alongside surface forcing to water mass transformation. Therefore we aim to fill these gaps in our knowledge. The structure of this paper is as follows. Section 2 describes our approach (our reasons for our choice of methods) and outlines our methods and data, and Section 3 presents our results and uncertainties. In Section 4, we discuss the significance of the results both in present terms and against likely future changes in the Arctic.

2. Data and Methods

2.1. Approach

Our aim is to diagnose net Arctic Ocean water mass transformation rates, meaning the rate of change of a water parcel's density. Density can be changed in two main ways: by fluxes of density at the surface, and by turbulent diapycnal mixing in the ocean interior. We choose to use the term "density flux": although it has units of kg s⁻¹ (as described in Sections 2.2 and 2.3), and while most processes are physical movements of mass (ocean boundary advection, surface freshwater addition from river runoff, or the work done by turbulent mixing forcing lighter waters downwards and denser waters upwards), the key process of heat loss entails no such movement of mass. As a consequence, we will present profiles of pan-Arctic water mass transformation rates resolved by density. Depth is not appropriate as a coordinate because different densities are found across similar depths. In addition, we avoid the term "buoyancy," which is (effectively) the opposite of density. Buoyancy loss is density gain, and vice-versa. Note also that we will abbreviate "turbulent diapycnal mixing" to "turbulent mixing" in what follows.

The present study is an extension of T2012, whereby the Arctic Ocean is treated as a control volume, in which the top and bottom boundaries are the sea ice or ocean surface and the seabed, respectively; the side boundaries are the four ocean gateways of Fram, Davis and Bering Straits and the Barents Sea Opening, and land (Figure 1). Here, density levels form internal ocean boundaries, and we choose a set of 30 density levels to span the water column (Table 1), so that adjacent pairs of levels form density layers. Key density levels are chosen to match the water mass definitions of T2012, which are also noted in Table 1. T2012 also provide a concordance (their Table 1) between the chosen water masses and other naming conventions employed in the literature.

Our ambition is to calculate representative, annual-mean water mass transformation rates within the control volume and for each density layer, and we discuss the interpretation of timescales in Section 4. First, we calculate water mass transformation rates at the surface and for each layer within the control volume caused by surface fluxes of heat and freshwater (Section 2.2), which requires sub-annual resolution of surface fluxes, because winter surface forcing creates high-density waters, while density reduction happens in summer. The amplitudes of Arctic surface seasonal cycles (e.g., Bacon et al., 2015; Mayer et al., 2019; Serreze et al., 2007) mean that application of annual-mean forcing to annual-mean surface properties would mislead. Second, having calculated surface-forced water transformation rates, we apply a box model to each layer bounded by the control volume to calculate a profile of net interior turbulent mixing rates (Section 2.3) versus density. Note that we will use ρ for density in what follows, but all calculations employ ocean potential density referenced to the surface, σ_0 .

BROWN ET AL. 4 of 22

Table 1Box Model Density (σ_0) Levels, Their Mean Depths, the Water Masses as Described by T2012 With Abbreviations Subsurf (Subsurface), Intermed (Intermediate), and Atl (Atlantic); Other Columns Are Described in Section 3

Density level	$\sigma_0 (\mathrm{kg} \; \mathrm{m}^{-3})$	Mean depth (m)	Water mass	$D_{\rm diff}~(\times 10^4~{\rm kg~s^{-1}})$	$D_{\rm surf} (\times 10^4 {\rm \ kg \ s^{-1}})$	Advective flux (kg s ⁻¹)	Diffusivity ($\times 10^{-6} \text{ m}^2 \text{ s}^{-1}$)
30	24.7	20	Surface	52.14	15.38	3.68E+5	1.16
29	25.1	27		83.80	37.13	4.67E+5	1.81
28	25.5	37		107.87	53.60	5.43E+5	2.57
27	26.0	53		131.95	69.43	6.25E+5	4.41
26	26.4	71	Subsurf	159.35	80.47	7.89E+5	6.65
25	26.7	83		180.67	94.05	8.66E+5	8.89
24	26.9	93		180.58	99.63	8.10E+5	10.44
23	27.0	98		176.59	102.23	7.44E+5	11.08
22	27.1	106	Upper Atl	171.12	106.77	6.44E+5	11.64
21	27.3	121		146.52	107.84	3.87E+5	12.14
20	27.5	145	Atlantic	99.82	93.05	6.77E+4	11.80
19	27.55	153		85.39	87.59	-2.20E+4	11.62
18	27.58	158		77.42	84.65	-7.23E+4	11.67
17	27.6	161		71.22	81.52	-1.03E+5	11.60
16	27.7	196		42.73	63.12	-2.04E+5	10.90
15	27.8	194		17.96	38.72	-2.08E+5	8.65
14	27.84	213		9.10	27.10	-1.80E+5	5.74
13	27.88	239		3.37	16.82	-1.35E+5	3.15
12	27.9	259		3.24	13.98	-1.07E+5	3.90
11	27.921	284	Intermed	3.07	10.82	-7.75E+4	4.88
10	27.948	337		3.27	7.31	-4.04E+4	8.13
9	27.962	382	Deep	2.83	5.29	-2.45E+4	9.09
8	27.986	493		1.97	2.31	-3.37E+3	9.01
7	28.010	630		1.19	0.36	8.31E+3	7.43
6	28.037	863		1.33	0.34	9.91E+3	12.71
5	28.050	1,067		1.06	0.34	7.15E+3	12.84
4	28.060	1,262		0.74	0.33	4.12E+3	11.34
3	28.070	1,490		0.36	0.29	7.55E+2	7.17
2	28.076	1,580		0.23	0.30	-7.05E+2	5.01
1	28.087	1,958		0.34	0.34	-3.89E-1	13.68
0	Seabed	Variable					

2.2. Surface Density Fluxes

The profile of diffusive surface density flux, D_{surf} , is calculated using the formulation of Jullion et al. (2010). Between each pair of densities that define layer n, $D_{\text{surf},n}$ (kg s⁻¹) is given by:

$$D_{\text{surf},n} = \frac{1}{12} \sum_{j=1}^{12} \int_{A_{\text{surf},n}^{j}} \left(\frac{\alpha Q_n^j}{c_p} - \left[\overline{\rho}_{\text{surf},n}^j \beta F_n^j \overline{S}_n^j \right] \right) dA$$
 (1)

where A is horizontal area. Each outcropping layer n is delimited by each pair of densities. Then $A_{\text{surf},n}$ is the outcrop area of layer n, α is the thermal expansion coefficient for seawater (°C⁻¹), Q_n is the air-sea net heat flux per unit area (W m⁻², +ve into the ocean) for the outcrop, c_p is the specific heat capacity of seawater (J kg⁻¹ °C⁻¹), $\overline{\rho}_{\text{surf},n}$ is the outcrop's mean surface density, β is the haline contraction coefficient for seawater, F_n is the surface

BROWN ET AL. 5 of 22

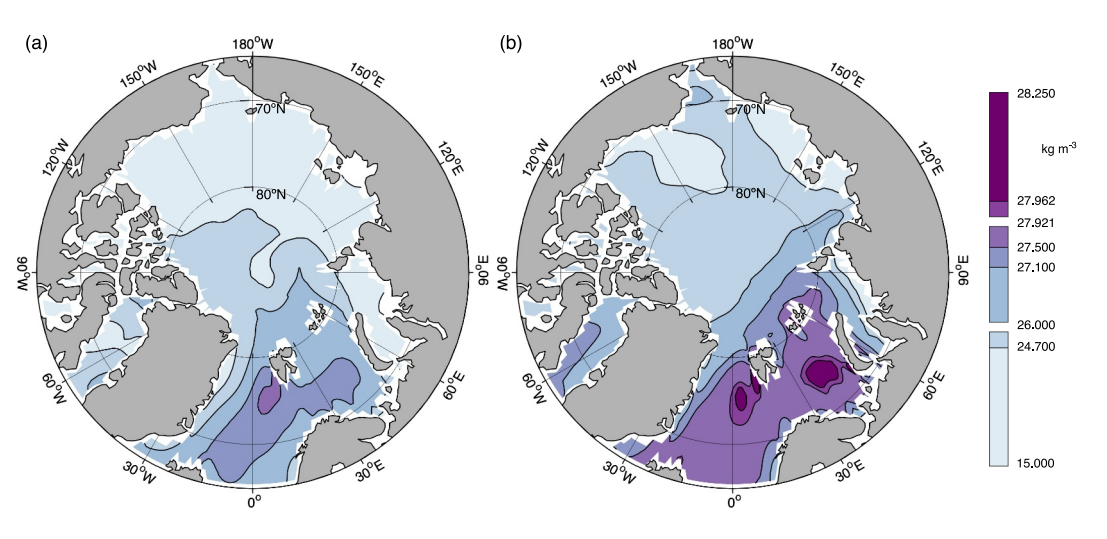


Figure 3. Sea surface densities (σ_0) calculated from PHC 3.0 temperature and salinity fields for (a) September and (b) March.

freshwater flux per unit area into the outcrop (m³ s⁻¹, +ve into the ocean) that arises from the net of precipitation (P), evaporation (E) and river runoff (R), and \overline{S}_n is the outcrop's mean surface salinity. The calculation is performed for each layer for the 12 months of the year (superscript j) and then summed and averaged. Finally D_{surf} is then the density-resolved annual-mean profile of surface density flux within the control volume.

We choose two reanalysis products, ERA-Interim (provided by the European Center for Medium-Range Weather Forecasts; Dee et al., 2011) and Modern-Era Retrospective Analysis for Research and Applications (the MERRA, provided by NASA; Rienecker et al., 2011) for components of surface forcing and for sensitivity testing. Lindsay et al. (2014) identified both products as being consistent with independent observations. Monthly average fields for surface net solar radiation, surface net thermal radiation, surface latent heat flux and surface sensible heat flux at 1.0° resolution are summed to obtain estimates of total heat flux per unit area (*Q*). The annual-mean surface heat flux within the control volume is *ca.* 200 TW (ocean to atmosphere), compared to the sea ice freeze/melt heat flux *ca.* 25 TW (Bacon et al., 2015; Serreze et al., 2007), because the majority of surface heat fluxes occur over the warmer, ice-free waters of Atlantic origin in the eastern part of Fram Strait and the Barents Sea (Serreze et al., 2007). To simplify, therefore, we choose to apply heat fluxes directly to the liquid ocean surface. However, this disregard of sea ice introduces an uncertainty in our calculations, so we consider it further in Section 3.2.

To generate the surface freshwater flux F, monthly ERA-Interim and MERRA fields for E and P are combined to give the P-E component of freshwater flux F. In each case, fluxes are scaled by the ERA-Interim field for proportion of ice-free water, although this might lead to some under-counting of freshwater input to the upper layers, if precipitation—that is not included in the flux estimates because it falls over ice-covered ocean—subsequently thaws and enters the ocean during the late summer melt period. The Arctic Ocean Model Inter-comparison Project (AOMIP) river runoff data set provides monthly total (gauged plus ungauged) values of R (Figure 2; Prange and Lohmann, 2004). River outflow is assumed to be distributed by advection across the continental shelves (defined as having water depth less than 400 m). The monthly average AOMIP fluxes are distributed evenly by area to surface grid cells on the Canadian shelf west of 120°W and the Siberian shelf east of Novaya Zemlya (ca. 60°E). The rate of land-to-ocean mass loss from the Greenland Ice Sheet is negligible for our study period, at a total of a few tens of km³ yr $^{-1}$ (IMBIE Team, 2020).

Monthly surface density and salinity data are calculated and obtained from the monthly temperature and salinity fields of the Polar Science Center Hydrographic Climatology (PHC) v. 3.0 (updated by the originators from Steele et al., 2001). The areas of integration of surface fluxes in Equation 1 are calculated from monthly sea surface densities, illustrated for September and March (Figure 3). The horizontal resolution of PHC data is 1.0°, so some areas up to *ca.* 100 km from the coast are excluded as a result. However, with the exception of coastal waters to the north and west of Svalbard and around Franz Josef Land, these are limited to regions where only the surface water classes outcrop (Figure 3).

BROWN ET AL. 6 of 22

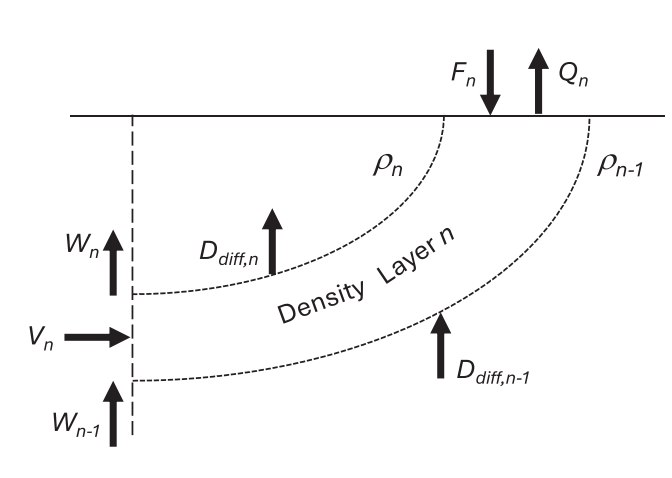


Figure 4. Box model sketch for the *n*th density layer within the control volume. Shown are the sea surface (horizontal line), the ice-ocean boundary (dashed vertical line) and two adjacent density levels, ρ_n and ρ_{n-1} , as curved dashed lines. The components of the layer volume budget are the horizontal flux V_n at the ice-ocean boundary, the surface freshwater flux F_n , and the diapycnal fluxes W_{n-1} and W_n calculated at the ice-ocean boundary and resulting from water mass transformations. Density fluxes due to diapycnal mixing are shown as D_{diff} for each density level. The layer's surface density flux, $D_{\text{surf},n}$, is calculated from F_n and the surface heat flux, Q_n . The layer's total density budget is calculated from all terms.

ERA-Interim reanalysis fluxes and AOMIP river runoff estimates are integrated by month over the outcropping area of each density layer as derived from the PHC climatology. The principal calculations use data for the months from September 2004 to August 2005, the year leading up to the period in which the boundary observations used for the derivation of the velocity estimates were made (Section 2.3). To test sensitivity of variability in heat fluxes, the calculations are repeated with data for the previous year, September 2003 to August 2004. A further sensitivity test is conducted for 2004–2005 using MERRA reanalysis data in place of ERA-Interim.

2.3. Diffusive Density Fluxes

To calculate the profile of rates of net Arctic Ocean turbulent mixing, we apply a box model (Figure 4) to the control volume of Figure 1. We first calculate the volume budget for layers defined by a density level as the upper surface and the sea bed as its lower surface. For each layer n, the net diapycnal volume flux, W_n , into or out of the layer is then:

$$W_n - W_{n-1} = V_n + F_n (2)$$

where V_n is the net layer volume flux through the side boundary and F_n is the surface volume flux to the layer's surface outcrop from input of freshwater, and where F = P - E + R. All terms are in m³ s⁻¹.

For each density layer n, the boundary volume flux V_n is:

$$V_n = \oint \int_{z_{n-1}}^{z_n} v \, dz \, dx \tag{3}$$

where v = v(x,z) is velocity normal to the boundary, x is the along-boundary coordinate, z is depth, and the circuit integral is taken around the full boundary (x). The limits of integration are $z_n = z(\rho_n)$, the depth of the relevant density level, with density $\rho = \rho(x,z)$. The lower limit is either the isopycnal depth, or the seabed, if the density layer grounds. The upper limit is the either the relevant isopycnal depth, or the sea surface, if the density layer outcrops. The bottom layer is the sea bed, assigned n = 0 and where $W_0 = 0$, so that the profile of values of W is calculated from the bottom (most dense layer) upwards. Note that W values are the net rate of volume transfer between density layers as observed at the ice-ocean boundary of the control volume and as the net result of water mass transformations caused by surface fluxes and mixing in the interior of the control volume. W values do not represent interior vertical velocities.

To calculate the diapycnal mixing rates needed to maintain the Arctic Ocean stratification, we calculate density budgets for each density layer. We use the formulation of Walin (1982) as adapted for density transformations by Large and Nurser (2001), whereby (in the steady state) diapycnal water mass transformations at (or near) the surface must be balanced by water mass transformations deeper in the water column, while these two forcings on density must be represented by their the net impacts on diapycnal mass (volume) transfers between layers as measured around the faces of the box. Our calculations produce, within the control volume, area-mean diapycnal diffusive density fluxes, $D_{\rm diff}$, as a functions of density class. Large and Nurser (2001) derive the density budget (kg s⁻¹) for each density layer as:

$$D_{\text{diff},n} - D_{\text{diff},n-1} = \oint \int_{z_{n-1}}^{z_n} \rho v dz \, dx - \left(\rho_n W_n - \left[\rho_{n-1} W_{n-1}\right]\right) + \overline{\rho}_{\text{surf},n} \, F_n + D_{\text{surf},n} + \Delta \tag{4}$$

where $D_{\text{diff},n}$ is the diffusive flux of density into or out of layer n, over the whole of the density level within the control volume. The first term on the RHS is the boundary mass budget for density layer n, and where the limits of integration are as for Equation 3. The second term is the layer's net change of mass caused by exchanges with adjacent layers of greater or lesser density. The third term is the surface mass flux due to freshwater input, with

BROWN ET AL. 7 of 22

from https://agupubs.onlinelibrary.wiley.com/doi/10.1029/2024AV001529 by NICE, National Institute for Health and Care Excellence, Wiley Online Library on [18/11/2025]. See the Terms

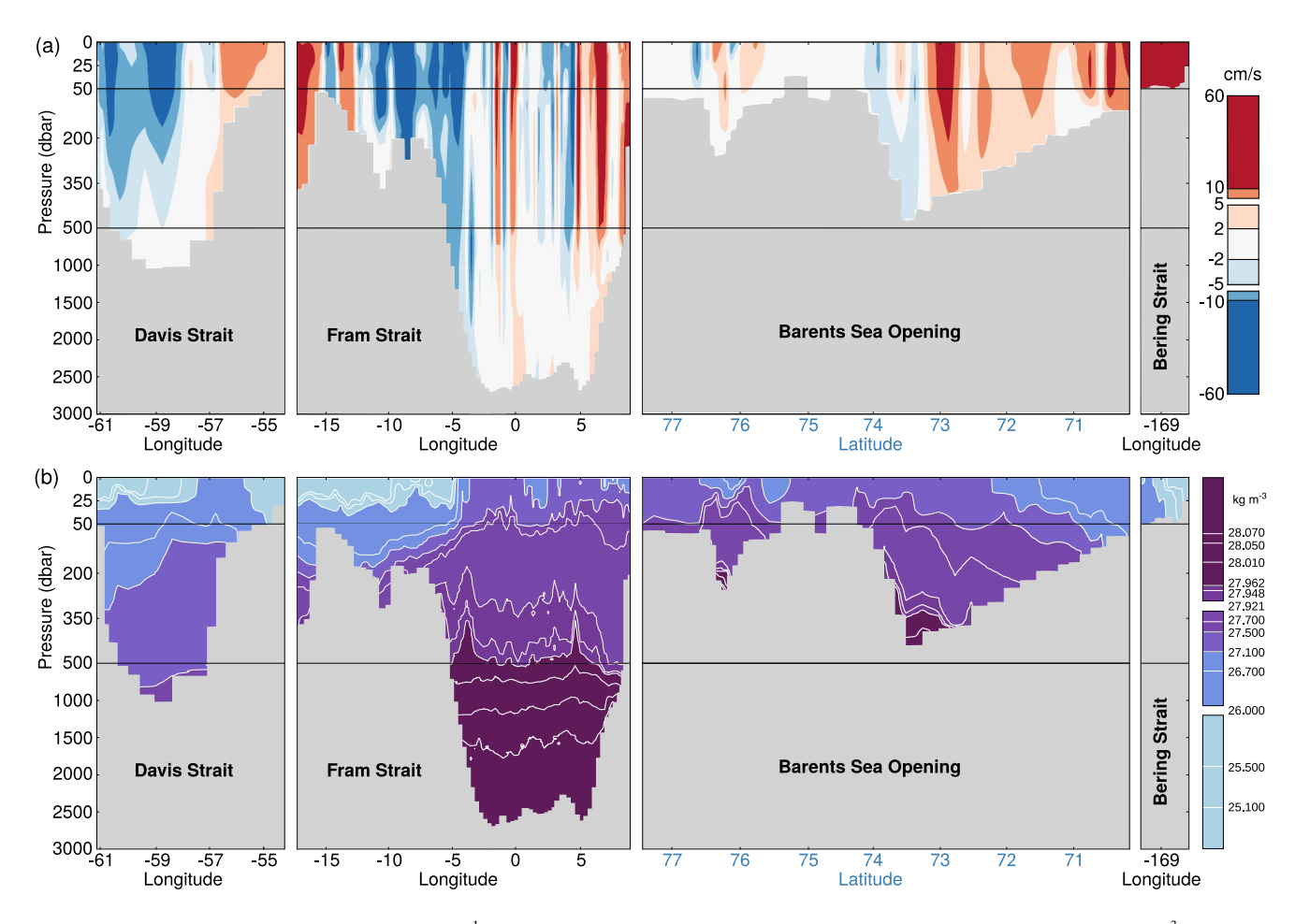


Figure 5. Arctic Ocean boundary section. (a) Velocity (cm s⁻¹), inflows to Arctic are positive (red), outflows negative (blue); (b) density as σ_0 (kg m⁻³); see Table 1 for full list of density levels.

 $\overline{\rho}_{\text{surf},n}$ the layer's mean density at the sea surface. D_{surf} is obtained as above in Equation 1. Interior sources of density, such as cabbeling, are represented by Δ . The bottom layer is the sea bed, assigned n=0 and where $D_{\text{diff},0}=0$, so that the profile of values of D_{diff} is calculated from the bottom (most dense layer) upwards. We comment further on the formulation of Equation 4 toward the end of Section 3.1.

Turning now to data sources, the boundary velocities used in the calculation of boundary volume fluxes and boundary densities are obtained from T2012, which they derive using an inverse model applied to quasi-synoptic ocean and sea ice observations made across the four main gateways to the Arctic Ocean (Bering, Davis and Fram Straits and the Barents Sea Opening). The utility of the data set has been demonstrated in several previous studies (reviewed in Bacon et al., 2022). We choose to use it here because it is the only existing high-quality, high-resolution (in both vertical and horizontal) source of coast-to-coast and surface-to-sea-bed Arctic Ocean boundary density data. Measurements were collected by ship-borne and mooring-based instruments over the period 9 August to 10 September 2005. To fill in short distances at the landward ends of the Barents Sea Opening where observational data were not available, these were supplemented with output from a high-resolution coupled ice-ocean general circulation model. The inverse model was constrained to conserve volume and salinity anomaly, and the resulting velocities were interpolated onto a 10 dbar vertical grid. The horizontal circulation is reasonable, as discussed in T2012. The longer-term (but lower spatial resolution) studies of Tsubouchi et al. (2018, 1 year; 2024, 5 years) enable consideration of uncertainties resulting from this choice of data set in Section 3.2. Density and velocity fields are shown in Figure 5; see T2012 (their Figure 5) for temperature and salinity fields.

BROWN ET AL. 8 of 22

While surface freshwater fluxes were a diagnostic output from the T2012 inverse model, in the present study, we impose surface fluxes F as calculated in Section 2.2. Therefore to re-impose full-depth volume conservation, we apply a uniform, barotropic correction to ocean velocities, of order 1×10^{-4} m s⁻¹. These adjustments have negligible effects on all calculations: for example for a layer 100 m thick and 500 km wide, the resulting transport uncertainty is 5×10^3 m³ s⁻¹ (0.005 Sv). Horizontal transports into and out of the ice-ocean boundary are therefore effectively the same as in T2012.

Cabbeling results from the mixing of water masses of the same density but differing temperatures and salinities, and is caused by nonlinearities in the equation of state. Isachsen et al. (2007) note that interior sources of density are of secondary importance in high-latitude dense water production regions. Lobb et al. (2003) examined a front in Baffin Bay where Atlantic-sourced waters encounter cold, fresh Polar waters, and found a maximum increase in density from cabbeling of $\sim 0.01 \text{ kg m}^{-3}$ around density 27.5 kg m⁻³. The effect is small, so we do not include it in our water mass transformation calculations.

The diffusive flux of density is expressed as a net, basin-mean diffusivity, κ :

$$\kappa_n = -\frac{D_{\text{diff},n}}{A_n \frac{\partial \rho_n}{\partial r}} \tag{5}$$

where, for each layer n, A_n is the surface area of the relevant density level forming the layer's upper boundary and $\partial \rho_n / \partial z$ the mean density gradient across the density level. Both parameters are calculated over the interior of the control volume using the PHC data set. Monthly PHC temperature and salinity fields are available for depths down to 1,500 m. For greater depths, we use summer (July, August, September) means, which is acceptable because seasonal signals are not known to penetrate to these depths (Lique & Steele, 2012). Areas and density gradients are shown in Figure 6. Calculation of diffusivities constitutes our only use of ocean-interior data.

Results are presented with the following sign conventions. For volume transports, V is positive for transports into, and negative out of, the control volume; W is positive-upwards; and F is positive into the surface. For density fluxes, $D_{\rm surf}$ is positive for addition of density at the surface, that is heat loss, and negative for removal of density, that is for heat and freshwater gain. $D_{\rm diff}$ is the mixing term; with $d\rho/dz$ always negative (decreasing upwards), mixing always causes a positive flux of density upwards (equivalent to a downwards flux of lighter water), so that the upwards density flux due to mixing is signed positive. With allowance for sign conventions, Equation 4 states (a) that for any layer, the density budget is quantified by the net of inflows to and outflows from the layer, at the sides (V), surface (F) and from layer to layer (W)—these terms are called "advective"—and (b) that the causes of these changes to density fluxes are quantified in part by surface fluxes $(D_{\rm surf})$, finally enabling calculation of interior turbulent mixing rates $(D_{\rm diff})$.

3. Results

3.1. Overturning, Surface Forcing and Interior Mixing

Net Arctic Ocean diapycnal volume transports (W) express the net transfers of volume between density layers caused by water mass transformation processes, and are shown in Figure 7. Divergent diapycnal transports (dW/dz > 0) are seen at densities 27.5 < $\sigma_0 < 27.9$ kg m⁻³, that is throughout the Atlantic Water layer. The strongest upward transport is 1.8 Sv, which occurs across $\sigma_0 = 27.5$ kg m⁻³, the boundary between Atlantic Water and Upper Atlantic Water, and the strongest downward transport is 1.5 Sv, across $\sigma_0 = 27.9$ kg m⁻³, the base of the Atlantic Water layer. The net effect is to transform nearly half of the inflowing Atlantic Water layer into lighter and denser classes. Convergent diapycnal transports (dW/dz < 0) are seen above and below the Atlantic Water layer, where 26.4 < $\sigma_0 < 27.5$ kg m⁻³ and where 27.92 < $\sigma_0 < 28.06$ kg m⁻³ (respectively). These layers gain water and export more than they import. The lightest Surface Waters, where <26.4 kg m⁻³, are near-non-divergent ($dW/dz \sim 0$), with downward transports reflecting positive surface volume fluxes from net freshwater addition (F). The resulting dominant impression centers on the fate of the inflowing Atlantic Water: part is transformed into lighter water and part into denser water, demonstrating the existence of the two-cell overturning circulation—the double estuary. The change from convergence to divergence occurs in the Atlantic Water layer at $\sigma_0 = 27.75$ kg m⁻³.

BROWN ET AL. 9 of 22

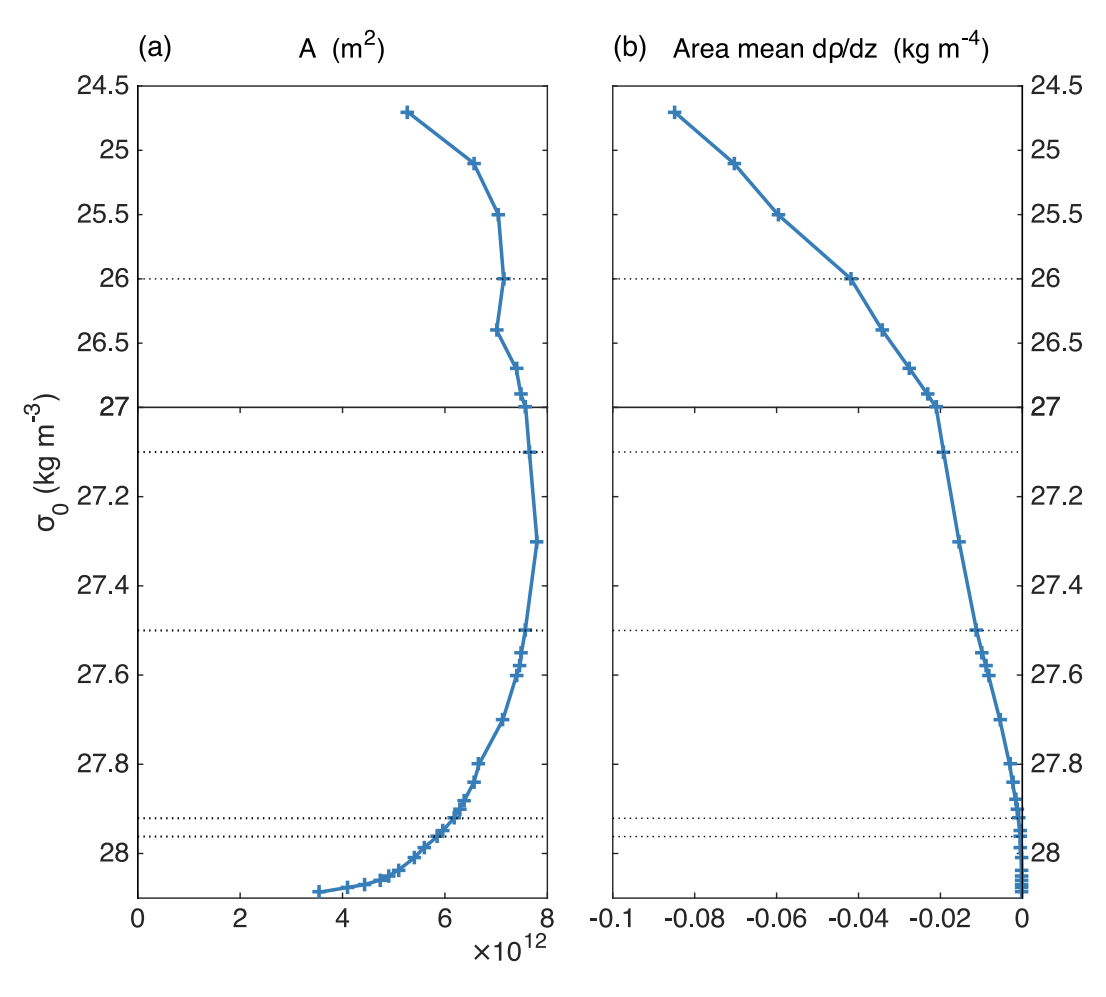


Figure 6. (a) Isopycnal surface areas (A) and (b) basin-mean density gradients $(d\rho/dz)$, both as σ_0 calculated from the PHC 3.0 climatology.

We next inspect the contribution of surface forcing to these water mass transformations, beginning with the annual-mean heat and freshwater contributions to surface density fluxes for the period September 2004 to August 2005 (Figure 8). In the annual mean, the dominant process is densification due to heat loss, which is concentrated in the south-western Barents Sea where warm, inflowing Atlantic Water is present at the surface throughout the year. Smaller and weaker areas of annual-mean density gain and loss are minority contributors. There is an annual-mean density loss due to net freshwater input that reflects the distribution adopted for river runoff, and is dominated by river input on the Siberian shelves.

Considering the seasonal cycle of surface density fluxes (Figure 9), heat loss affects only the lightest density classes in September 2004, but as the winter progresses, the loss of heat from the surface increases the volume converted to increasingly dense layers, which begin to outcrop. The densest waters ($\sigma_0 \sim 28.0 \text{ kg m}^{-3}$) gain volume at the surface in March 2005. From January until the end of winter, Surface Waters experience limited surface fluxes because the ice cover inhibits transfer of heat between atmosphere and ocean. From May through the remainder of the summer, heat is gained by the ocean and density lost, with the waters in contact with the atmosphere becoming progressively less dense. Averaged over the year, the bulk of the effect of surface heat fluxes is a densification of part of the inflowing Atlantic Waters—with some densification also affecting Upper Atlantic Waters—so that they are transformed into Intermediate and Deep Waters.

Spring melting causes a rapid increase in river runoff through May to its maximum in June, followed by a steady decrease through to the following winter (Figure 2). Monthly mean surface density fluxes due to freshwater are consistently smaller in magnitude than those due to heat flux for all layers apart from the lightest surface water, but because they remove density from the ocean (i.e., they add buoyancy), averaged over the year they give rise to

BROWN ET AL. 10 of 22

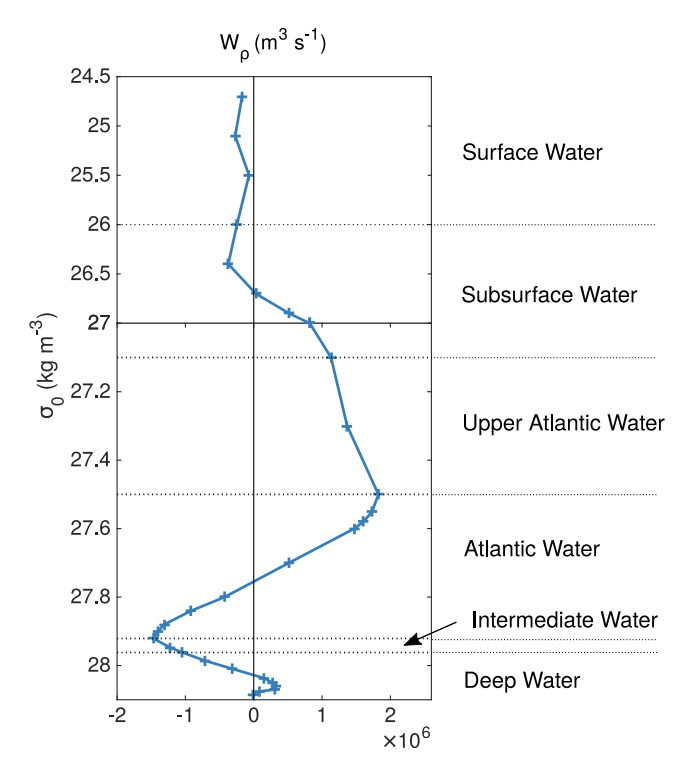


Figure 7. Diapycnal volume transports (*W*) across each isopycnal layer boundary (blue). Transports from denser to less dense layers (i.e., upwards) are positive. The density scale changes at $\sigma_0 = 27.0 \text{ kg m}^{-3}$.

density fluxes of similar magnitude to those produced by heat fluxes in the Surface Water layer. For Atlantic and Upper Atlantic Waters, however, the effect of freshwater fluxes is negligible, because they are exposed to the surface in the Barents Sea and eastern Fram Strait, remote from the major riverine sources of freshwater.

The final step is to calculate the profile of interior diffusive fluxes of density $(D_{\rm diff})$ as the sum of the three advective terms in Equation 4 and the surface density flux (D_{surf}) , shown in Figure 10a, with the calculated turbulent diffusivities (Equation 5) in Figure 10b; all values are presented in Table 1. Note that the sign of D_{surf} is a consequence of our formulation of Equation 4; its sign would be reversed had Equation 4 been written thus: total water mass transformation rate = D_{surf} plus D_{diff} = the sum of advective terms. The density budget requires diffusive density fluxes that are very small (ca. $1 \times 10^4 \,\mathrm{kg \, s^{-1}}$) in the Deep and Intermediate Water layers. They then increase through the Atlantic and Upper Atlantic Water layers to reach a maximum of 1.8×10^6 kg s⁻¹ at $\sigma_0 \sim 26.7$ –26.9 kg m⁻³ in the Surface Water layer. Values then decline toward the surface, reaching $\sim 5 \times 10^5 \text{ kg s}^{-1}$. Diffusivities (κ) are $\sim 1 \times 10^{-5}$ m² s⁻¹ throughout much of the water column but decline toward the surface for densities $\sigma_0 < 27.0 \text{ kg m}^{-3}$, reaching $\sim 1 \times 10^{-6} \text{ m}^2 \text{ s}^{-1}$. There is a drop in diffusivity at the base of the Atlantic Water layer in Figure 10b. We attribute this to localized convection in the Barents Sea, which would have the effect of reducing the basin-mean values of diffusivity for these potential densities, but confirmation of this hypothesis is beyond the scope of this control volume-based study. The diffusivity variability in the deepest layers ($\sigma_0 > 28.0 \text{ kg m}^{-3}$) is an artifact of resolution: density fluxes (Figure 10a) and gradients (Figure 6b) are both small in this region.

Figure 10a shows that turbulent mixing is the dominant mechanism whereby less dense ocean waters and the surface input of freshwater (F) are mixed downwards, and equivalently, denser waters are mixed upwards—where "upwards" and "downwards" also mean toward less or more dense waters (respectively)—so that volume is transferred from denser to less-dense layers. $D_{\rm diff}$ becomes significant for densities where $\sigma_0 > ca$.

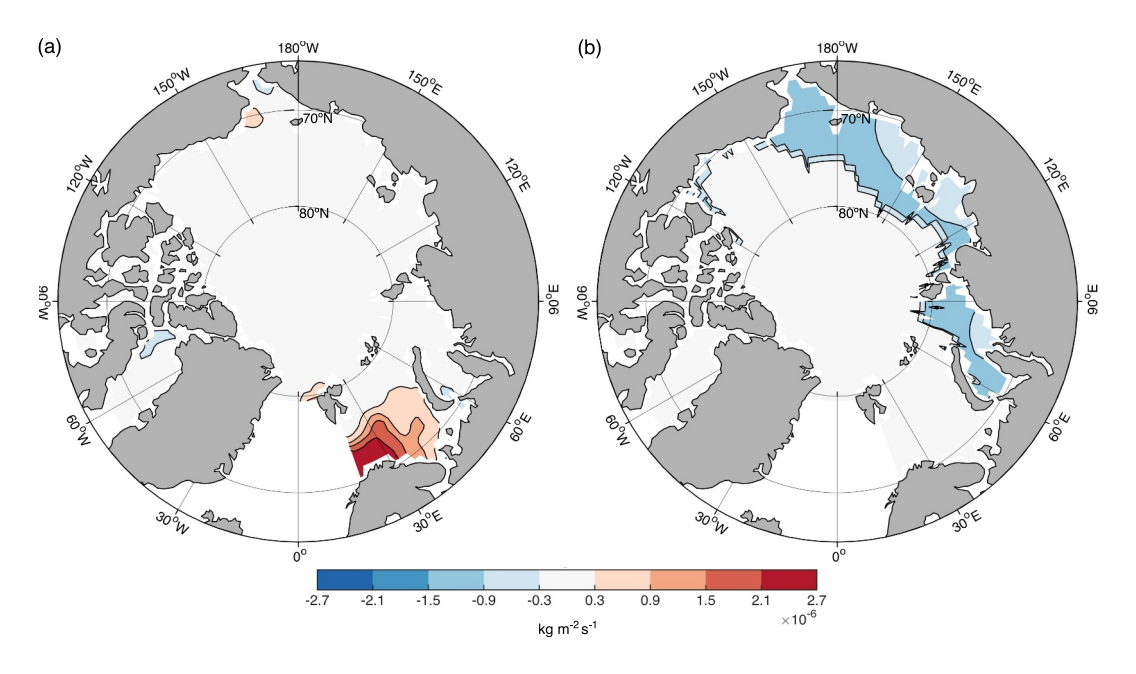


Figure 8. Annual mean surface density flux per unit area due to (a) net heat flux and (b) net freshwater flux. Positive values indicate addition of density to the ocean.

BROWN ET AL.

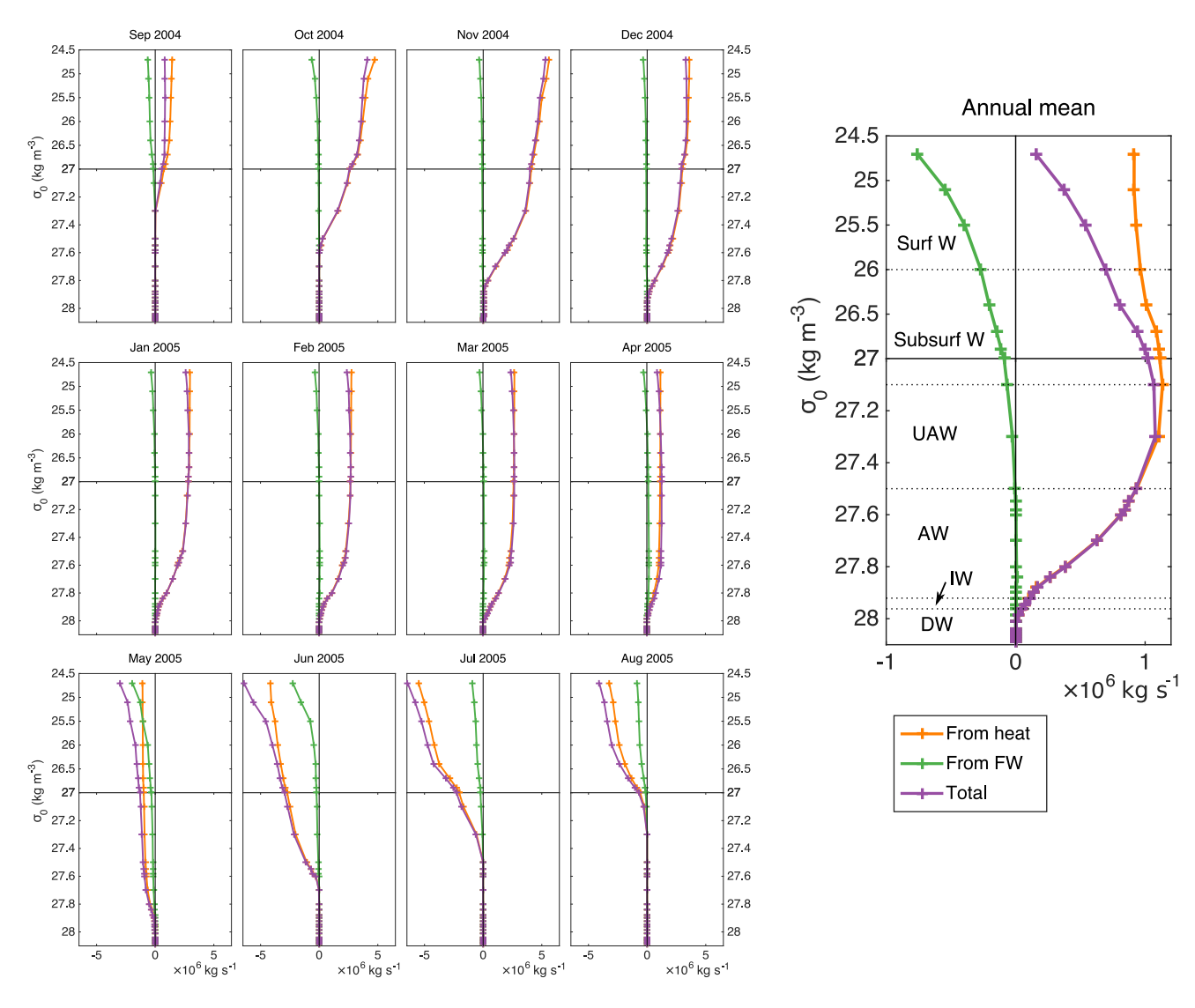


Figure 9. Monthly mean and annual area-integrated surface density fluxes, D_{surf}, for each isopycnal layer due to surface heat and freshwater fluxes.

27.7 kg m⁻³, the middle of the Atlantic Water layer, and it becomes larger than $D_{\rm surf}$ around $\sigma_0 = 27.50$ –27.55 kg m⁻³, the top of the Atlantic Water layer and into the base of the Upper Atlantic Water layer. Overall, therefore, the loss of volume from the Atlantic Waters, quantified above in the profile of W, is seen to be mainly due to (a) surface forcing increasing the volumes of denser waters by removing heat from Atlantic Waters and (b) turbulent mixing increasing the volumes of lighter waters by adding freshwater and less-dense ocean waters, to Atlantic Waters.

3.2. Robustness

Here we discuss (a) the vertical and horizontal transports (W and V), (b) inputs to the calculation of $D_{\rm surf}$, (c) the sea ice freeze/melt cycle, and (d) net uncertainties for $D_{\rm surf}$ and $D_{\rm diff}$.

First, for vertical fluxes (W), our maximum upward and downward transports out of the Atlantic Water layer are 1.8 and 1.5 Sv respectively. We compare these individual values with those of Tsubouchi et al. (2024), who generated a 5-year time series of monthly transports for the same control volume between October 2004 and May 2010 using sparser data from moorings, and who, thereby, generated uncertainty estimates expressed as the standard deviation (sd) of their monthly values about the mean. Their equivalent vertical transports are 1.4 ± 0.8 Sv upwards and 2.9 ± 1.2 Sv downwards. Our values of W are 0.5 sd higher (upwards) and 1.2 sd lower

BROWN ET AL. 12 of 22

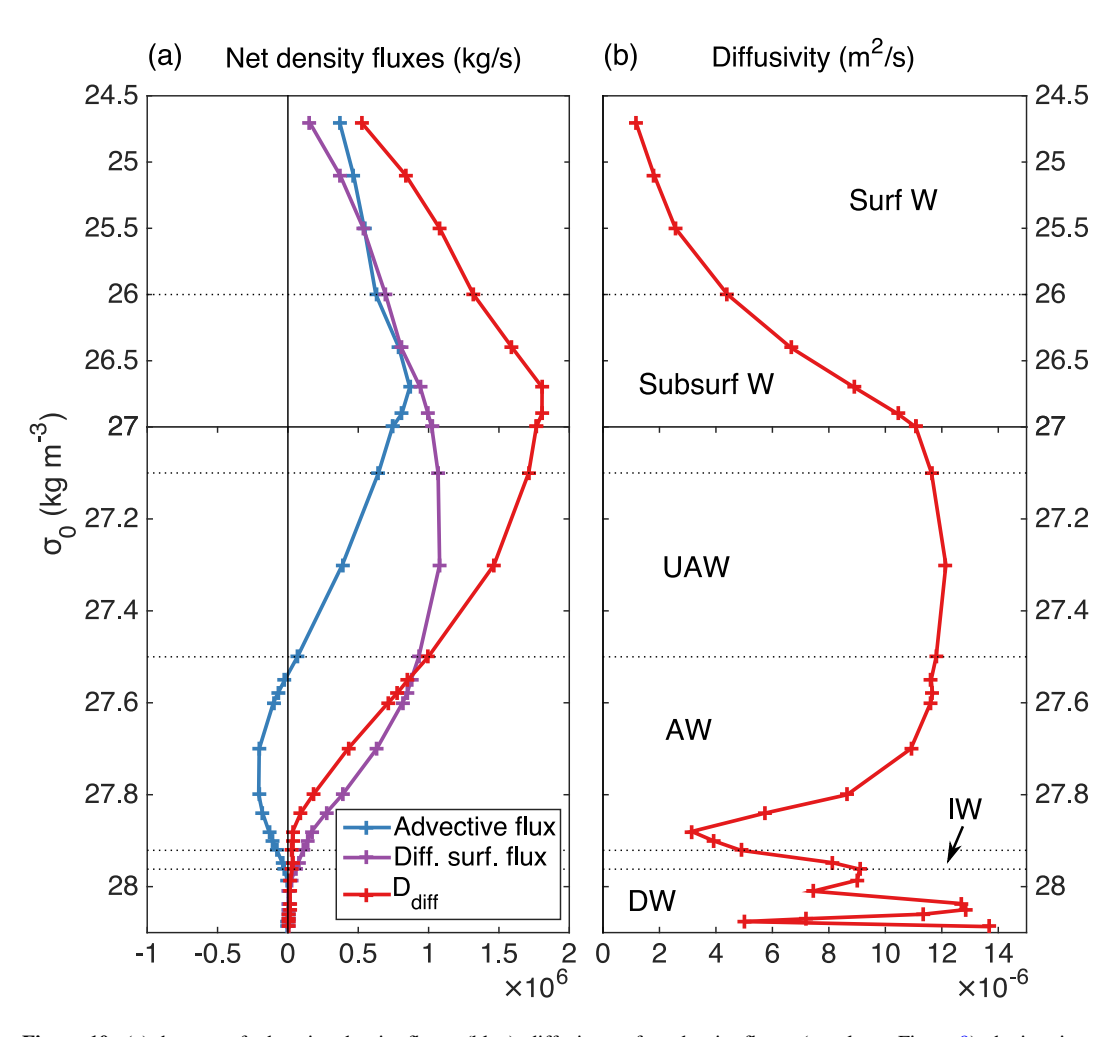


Figure 10. (a) the sum of advective density fluxes (blue), diffusive surface density fluxes (purple, as Figure 9), the interior diffusive flux of density, D_{diff} , (red). (b) Diffusivity (κ).

(downwards) than theirs. However, as Tsubouchi et al. (2024) observe, their "downwards" estimate is likely to be \sim 1.5 Sv too high: deep moored instruments in the west of Fram Strait capture the deep outflows, but the absence of deep measurements in the east of Fram Strait means that the outflows are not balanced by inflows. The inverse model's volume conservation constraints then force compensatory downwards flow from the overlying layer. Correcting for this unrealistic diapycnal transport means that their "downwards" value becomes ca. 1.4 Sv. As a consequence, our values of W are reasonable, that is within the observed range, and can be taken as characteristic of (at least) a 5-year mean. The Tsubouchi et al. (2024) W standard errors are ca. 0.1 and 0.2 Sv, so we use a conservative value of 0.4 Sv (ca. 25%) for our uncertainty in W. In addition, typical transport variability in horizontal volume transports V through the four gateways is ca. 50% (1 sd; Tsubouchi et al., 2024, their Table 2); as for W, we use a conservative 25% standard error uncertainty in V.

Second, we consider inputs to the calculation of surface density fluxes. The use of reanalyses to provide surface fluxes in the Arctic is known to be problematic because surface measurements to produce model constraints are sparse (Cowtan & Way, 2014), so that further exploration of reanalysis variability would ultimately confront this limitation. Mayer et al. (2019) show that rates of atmospheric energy convergence over the Arctic are similar, to within a few %, and for the period 2001–2015/2017 (their Table 2) for three reanalyses, ERA-Interim, the updated ECMWF product ERA5 and also for a Japan Meteorological Agency product (JRA-55), so that use of ERA-Interim as our primary reanalysis is reasonable.

Sensitivity of surface density fluxes to choice of reanalysis data set is shown in Figure 11. Repeating the reference calculations of Section 3.1 using (a) data from the same ERA-Interim product but a year earlier, and (b) a different

BROWN ET AL. 13 of 22

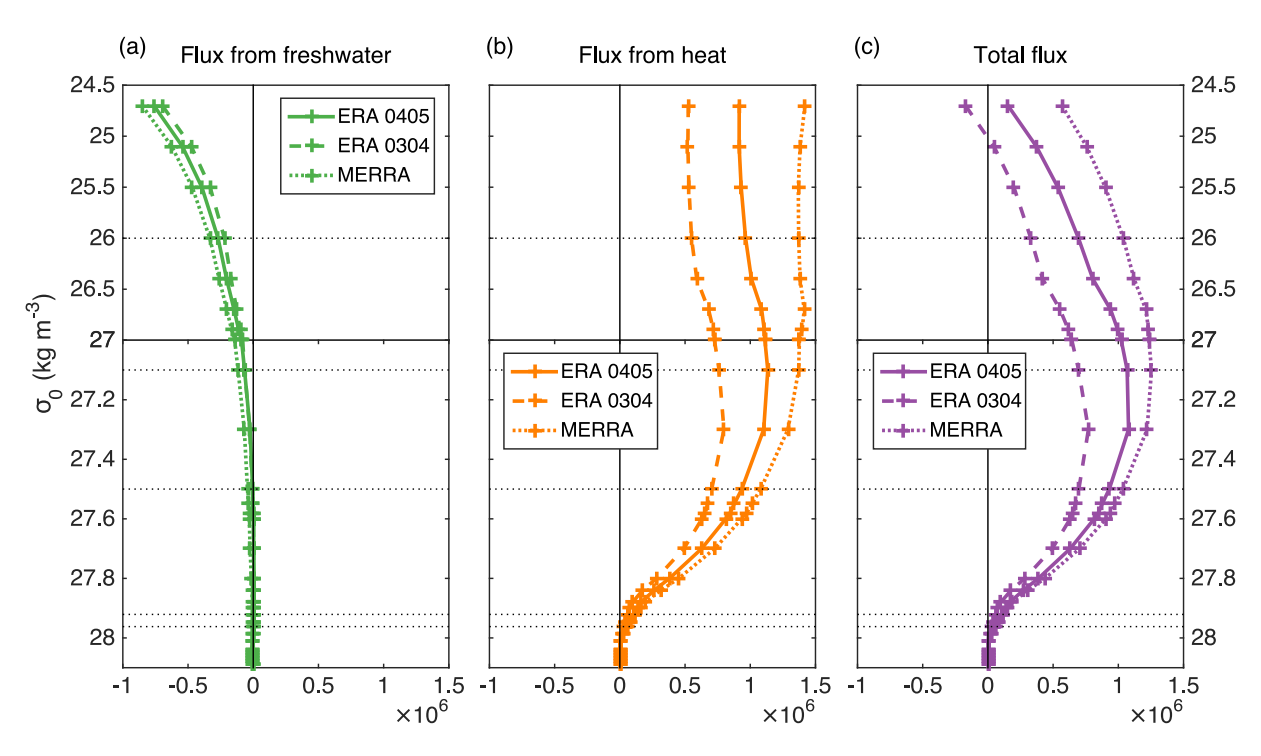


Figure 11. Comparison of surface density fluxes (kg s⁻¹) calculated using ERA-Interim reanalysis data for the years September 2004 to August 2005 (solid line) and September 2003 to August 2004 (dashed line), and MERRA reanalysis data for the year September 2004 to August 2005 (dotted line).

reanalysis product (MERRA) for the same year, results in heat flux contributions to density fluxes that are (a) lower and (b) higher than the reference values. The freshwater contributions are little changed because the net of P-E (obtained from the reanalyzes) is smaller than river runoff. The total density flux response is an approximate scaling of ca. $\pm 20\%$ (respectively) for densities greater than $\sigma_0 = 27.0 \text{ kg m}^{-3}$, while uncertainties become larger, perhaps 70%, for densities lower than $\sigma_0 = 27.0 \text{ kg m}^{-3}$ (roughly the upper 100 m—Table 1).

Mayer et al. (2019) constrain their improved Arctic energy budget with an early version of the ocean surface heat fluxes calculated by Tsubouchi et al. (2024), so that our results intersect with theirs. Mayer et al. (2019) also show variability in Arctic ice and ocean heat storage for several reanalysis products over the period 2001–2018 (their Figure 2). Given that Arctic Ocean advection timescales (from entry to exit within the control volume) are years-to-decades, the heat storage signal reflects surface heat flux and warm (Atlantic) water inflow variability. The trend illustrated by Mayer et al. (2019) equates to Arctic Ocean heat accumulation at \sim 7 TW (4 × 10²¹ J over 18 years), with interannual (to intra-decadal) variability up to half that at \sim 3 TW, and with comparable differences between products. The trend and variability are significant for ice and ocean behavior, but they are small in comparison to the mean surface heat flux of 180 TW (Tsubouchi et al., 2024) and the large seasonal surface heat flux cycle (e.g., Bacon et al., 2015). Overall, therefore, we take our uncertainties (above) to be a reasonable expression of structural (inter-model) and environmental uncertainty.

The PHC climatology is used to calculate monthly fields of Arctic Ocean surface densities and the surface areas contained within each surface density contour. We use PHC because it comprises data sourced from several decades prior to our measurement period in 2005, so there is some congruence between Atlantic Water circulation timescales (also decades: Wefing et al., 2021) and the PHC fields. However, it has no associated uncertainty estimates. We crudely estimate variability in surface areas using the (well-known) decline in sea ice extent (Cai et al., 2021; Stroeve & Notz, 2018) to represent change in surface ocean exposure to heat fluxes. The long-term rate of decline in sea ice is measured as 11.7% per decade for the summer minimum (September) and the winter rate (March) is 2.4% per decade. We choose a value of 10% to represent PHC surface area uncertainty as a result. Considering AOMIP, we estimate an additional river runoff (*R*) uncertainty of 10% from the interannual variability of the Shiklomanov et al. (2021) multi-decadal Arctic river discharge records. River inputs of sensible heat are negligible in the pan-Arctic context (e.g., Bacon et al., 2015).

BROWN ET AL. 14 of 22

Third, we do not consider explicitly the sea ice freeze/melt cycle in terms of its impact on heat fluxes between the atmosphere and the (liquid) ocean. As noted in Section 2.2, there is an order of magnitude difference between the annual-mean surface heat flux within the control volume versus the contribution from the rate of change of stored sea ice latent heat (freezing and melting)—ca. 200 TW versus 25 TW (Bacon et al., 2015; Mayer et al., 2019; Serreze et al., 2007). There is an interesting correspondence between the net sea ice latent heat production rate (the mean of 25 TW) compared with the same value of 25 TW for the mean latent heat exported by sea ice, which may be reasonable assuming the steady state. Considering the two seasonal surface heat flux cycles (about the mean), there is also a similar order of magnitude difference: seasonal amplitudes are ca.300 TW (range -100 to +500 TW, total surface heat flux) and -15 to 35 TW (range 10–60 TW, asymmetrical rate of change of sea ice stored latent heat).

It is reasonable to neglect to first order the sea ice component of surface heat fluxes, and we can estimate its impact from the heat content of the Arctic Ocean sea ice export rate of ~25 TW (Bacon et al., 2015; Tsubouchi et al., 2024). This is <15% of the total annual-mean surface heat flux, and is heat used in freezing that is not available for water mass transformation. Therefore, our surface-forced water mass transformation rates may be over-estimated in the net by ~15%, but this uncertainty is probably confined to the central Arctic Ocean because the denser Atlantic-sourced waters in the Barents Sea are ice-free (Figure 8). It is possible that the higher uncertainty of the impact on upper-ocean (σ_0 < 27.0 kg m⁻³) density fluxes of surface heat fluxes (Figure 11) is a reflection of this, if the bulk of the uncertainty is confined to the lower-density, mainly ice-covered upper-ocean waters of the central Arctic Ocean.

Finally, we estimate net uncertainties. We aggregate the uncertainties described above (root-sum-square). For $D_{\rm surf}$, combining uncertainties for PHC surface area (10%), river runoff (10%) and reanalysis (20%, with 70% for lighter waters) gives totals of 25% and 75%. For $D_{\rm diff}$, combining uncertainties for V (25%), W (25%), surface densities from PHC (10%) and $D_{\rm surf}$ (25%, with 75% for lighter waters) yields totals of 50% and 80% (lighter waters). We find that density budgets derived from advective fluxes and surface density fluxes produce estimates for turbulent diffusivity κ that appear realistic, excepting the variability in the densest layers. Given that the primary signal in κ is of an order-of-magnitude increase, from 10^{-6} m² s⁻¹ in the lowest-density layers near the surface to 10^{-5} m² s⁻¹ near $\sigma_0 = 27.0$ kg m⁻³, then decreasing again below $\sigma_0 = 27.8$ kg m⁻³, we consider the diffusivity profile in Figure 10b to be robust, in that it is representative of the integrated, pan-Arctic impact of turbulent mixing on water mass transformation. These are new results and direct comparators are not available. However, existing microstructure measurements (reviewed in Lenn et al., 2022) agree on the weakness ($\kappa \sim 10^{-6}$ m² s⁻¹) of diapycnal turbulent mixing for upper-ocean Arctic waters away from boundaries.

4. Discussion

In this Section, we first summarize our results, and consider timescales and uncertainties. We then examine two of the energy sources for turbulent mixing. We next broaden our perspective to include the Nordic Seas and the northern Atlantic MOC. To conclude, we place our results in the context of the recent past and of the changing future climate, and speculate on how future Arctic Ocean evolution might impact turbulent mixing.

4.1. Summary

We started from net water mass transformation rates observed around the ice-ocean boundary and manifested as changes in volumes transported by density layers. We then decomposed those rates into contributions from surface forcing and diapycnal mixing, and generated a pan-Arctic quantification of turbulent diffusivity from measurements. These results should be useful as baseline comparators against which model performance can be assessed, and they could provide integral constraints for Arctic Ocean state estimates.

The dominant process that forms Arctic Ocean dense waters is net heat loss to the atmosphere, which mainly happens to inflowing Atlantic waters in the central and southern Barents Sea. In contrast, inflowing waters are made less dense via the addition of freshwater at the surface, mainly by Siberian (and other) river runoff but also by the net of P–E and by ocean processes—the inflow of fresher, shallow ocean waters (through Bering Strait, and also off the coast of Norway), and the melting of sea ice where it encounters warmer Atlantic waters at the surface, near Svalbard and in the northern Barents Sea. The fresh waters then modify (by making lighter) inflowing denser waters mainly by turbulent mixing. It is likely that what makes the double estuary possible is geographical separation. The large surface heat fluxes that form dense waters occur in the Barents Sea, while the major sources

BROWN ET AL. 15 of 22

257 6604x, 2025, 6, Downloaded from https://agupubs.onlinelibrary.wiley.com/doi/10.1029/2024AV001529 by NICE, National

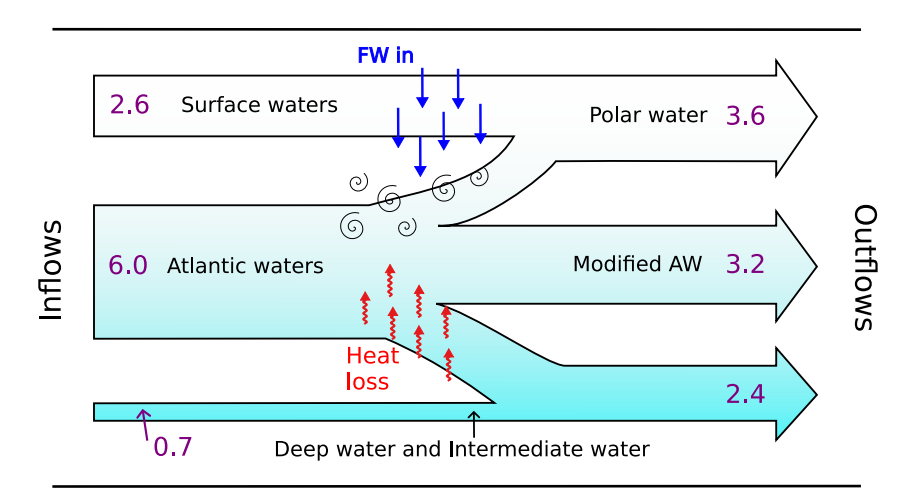


Figure 12. Schematic of the Arctic Ocean double estuary in density space, modified from Bacon et al. (2022), showing the consequences of water mass transformations. 1.8 Sv of the inflowing Atlantic waters are made denser by surface heat loss (red arrows), to add downstream to the Nordic Seas intermediate waters that together overflow the Greenland-Iceland-Scotland Ridge. 1.0 Sv of the Atlantic water inflows are made less dense by diapycnal turbulent mixing (spirals) of surface freshwater input (blue arrows), adding to the inflowing Surface waters, to be exported as Polar waters. Roughly half of the inflowing Atlantic waters are exported as modified Atlantic waters with little density change. The densest waters (0.7 Sv) recirculate within the combined system.

of freshwater input—rivers—initially impact the Siberian shelf seas. The weaker but more widely-spread surface-forced turbulent mixing that makes inflowing waters less dense then occurs in the Arctic Ocean, away from the Barents Sea. We summarize the double estuary in density space in Figure 12. The inflows and outflows are based on the calculations of T2012, noting the discussion of eddies and recirculations in Fram Strait in Bacon et al. (2022).

The impacts of the two processes—surface fluxes and turbulent mixing—are found to be of similar magnitudes. For lighter waters, the impact of turbulent mixing is about double that of surface fluxes, while for denser waters, surface fluxes are stronger than turbulent mixing, with the difference increasing with increasing density. This balance of processes is different in the Nordic Seas, where water mass transformation rates and the large-scale diapycnal overturning are largely described by surface forcing, and where turbulent mixing is secondary (Isachsen et al., 2007; Naveira Garabato et al., 2004).

4.2. Timescales and Uncertainties

A wide range of timescales is entailed by the Arctic Ocean circulation. Within the control volume, water mass conversion processes occur on surface forcing, circulation/advection and residence timescales that span perhaps five orders of magnitude. The shortest recirculation loops near the center of Fram Strait may only require weeks. Trans-basin surface ocean trajectories may have a timescale ~1 year (Wilson et al., 2021), while Atlantic Water layer transit times from entry to exit are a few decades, and for layers intermediate between the two, they may be from years up to a decade or two (Wefing et al., 2021). The longest timescales—centuries—apply to the deepest waters of the Canada Basin (Kipp et al., 2019). While seasonality occurs over months, Lique and Steele (2012) observe that the seasonal cycle accounts for a small or negligible part of Atlantic water temperature variability. To account for all timescales would require a study of a complexity beyond the present scope. However, the density transformation and diffusivity profiles likely represent increasingly longer timescales from least dense to most dense. Several decades ago, when dense water was still formed in the Greenland Sea by open-ocean convection that reached the sea bed (Bönisch et al., 1997; Karstensen et al., 2005), this would not have been true. Nevertheless, our interpretation is that the higher uncertainties for lower-density transformation rates result from the higher variability entailed by shorter timescales.

BROWN ET AL. 16 of 22

4.3. Energy Sources

Our results are, by construction, net quantifications that say nothing about the physical mechanisms by which mixing is accomplished. However, we can speculate on two of the sources of the energy supplied to turbulent mixing: (a) tides, and (b) heat, using calculations detailed in Supporting Information S1.

Our exploratory analysis quantifies the potential role of baroclinic tidal waves in generating some of the turbulence required to drive the Arctic Ocean basin-integrated interior mixing. We estimate the mechanical (tidal) power supplied to the small scales of 3-D turbulence, to provide depth-integrated (2-D) production rates of turbulent kinetic energy (TKE). We need to know how the TKE dissipation rate is distributed in the vertical, to partition the mixing between density layers, so we examine the sensitivity of our calculation to various plausible vertical profiles of TKE dissipation rate. Further sensitivity testing uses a theoretical model for the mixing efficiency; and we also consider the inclusion versus exclusion of the surface mixed layer, where wind and/or buoyancy forcing may dominate.

The total energy supply needed for mixing in the control volume is calculated (using $D_{\rm diff}$) as 2.2 GW. Restricting the calculation to the lighter water masses constituting the overturning's upper cell, this reduces to 1.3 GW. These values are dwarfed by the total tidal energy conversion within the Arctic, which integrates to 114 GW, although only up to ½ (the characteristic mixing efficiency of ocean turbulence; see Supporting Information S1) of this value—19 GW—will be expected to be available to drive mixing. This basic comparison suggests that tidally-generated turbulence is sufficiently energetic to make a large, possibly dominant, contribution to Arctic Ocean turbulent mixing in the present climate. The sensitivity testing shows that the different vertical distributions of tidal energy conversion rates have little impact on mixing, while changing the mixing efficiency (i.e., changing the fraction of tidal energy available to drive mixing) has the greatest impact for water masses denser than the Surface Water ($\sigma_0 > 27.0 \text{ kg m}^{-3}$). The influence of including versus excluding the surface mixed layer is of intermediate significance.

Overall, a consistent interpretation emerges, whereby tides supply sufficient energy to account for mixing in water masses where $\sigma_0 > 27.6 \text{ kg m}^{-3}$ (Atlantic Water and deeper). For lighter water masses where $27.0 < \sigma_0 < 27.6 \text{ kg m}^{-3}$ (Upper Atlantic Water), tides can potentially supply a majority of the energy requirement for basin-integrated mixing. Finally, for the lightest waters ($\sigma_0 < 27.0 \text{ kg m}^{-3}$; Surface Waters), tides make a minor contribution. This latter result accords with the greater exposure of upper-ocean waters to wind and sea ice stresses, and to thermodynamic forcings (particularly brine rejection during freezing), which could account for much of the required mixing there (see below).

Considering sea ice, the freezing-out of ice from seawater generates dense brines that drain from the sea ice. Being denser than the ambient seawater, the brine can then contribute to turbulent mixing. We infer that 0.35 GW is available to drive thermally-forced mixing in the Arctic Ocean—an order of magnitude smaller than the calculated 2.2 (1.3) GW total (upper-ocean) energy supply to Arctic Ocean mixing. This thermally-forced mixing is primarily focussed on near-surface waters that are exposed to the atmosphere in winter, so it is likely a major driver of mixing and overturning across those density classes.

This speculative analysis illustrates (a) the potentially major role played by tides in driving present-day Arctic Ocean overturning, (b) the particular importance of mixing efficiency in determining the extent of the tidal contribution, and (c) the magnitude and potential impact of thermally-forced mixing. Elucidating the magnitude of, and physics governing, mixing efficiency in the Arctic Ocean stands as a significant challenge for future research.

4.4. Nordic Seas and Northern North Atlantic MOC

The Arctic Ocean and the Nordic Seas both contribute to the formation of the dense "headwaters" of the Atlantic MOC. The well-known cartoon of the global MOC due to Broecker (1991) illustrates the northern Atlantic sector overturning (from shallow to deep water) with a single loop. Subsequent illustrations of the MOC have aimed for greater realism; for example Rahmstorf (2002) shows two descending loops. It is clear now that there are three loops when the Arctic Ocean dense water production is included with the northern North Atlantic and the Nordic Seas processes, in accordance with Zhang and Thomas (2021), who suggest that "the Arctic Ocean ... is the northern terminus of the mean Atlantic Overturning Circulation." The net dense water production rate in both the Arctic Ocean and Nordic Seas is ~6 Sv, from knowledge of the rate at which these waters overflow the shallow

BROWN ET AL. 17 of 22

(maximum depths 600–800 m) ridge between Greenland, Iceland and Scotland (Østerhus et al., 2019). Combining our results with those of Tsubouchi et al. (2021), the majority of this total of 6 Sv is generated in the Nordic Seas (~75%), and the remainder in the Arctic Ocean (~25%).

Broecker's single-cell or "two-legged" MOC does not apply to the Arctic, the Nordic Seas or Subpolar North Atlantic, by reason of the two-cell or "three-legged" circulation that results from the conversion to lower as well as to higher densities. The third leg is the export of cold, fresh waters from the Arctic and Nordic Seas into the northern North Atlantic to form the East and West Greenland Currents and the Labrador Current (and their allied Coastal Currents). These are all western boundary currents that are separate from the north-going, upper-ocean Atlantic waters in the eastern North Atlantic, and from the deep, dense, equatorward return flow at depth. The Subpolar North Atlantic is the subject of ongoing research in the OSNAP program (Lozier et al., 2017, 2019), but as noted in Section 1, changes in parts of the MOC in the Arctic and Nordic Seas can change the Subpolar MOC.

4.5. Recent Past and Future Climate Context

Our results derive from measurements made in 2005 at a time when the whole Arctic climate had begun to change. For most of recorded history, the Arctic Ocean has been covered by ice, winter and summer. As a result, the efficiency of atmosphere-to-ocean momentum transfer has been low, so that Arctic Ocean circulation has been sluggish, with typical speeds of a few cm s⁻¹, and turbulence has been quiescent, with upper-ocean diffusivities of order 10⁻⁶ m² s⁻¹. We cannot know whether our results are representative of previous ocean conditions, but we can tentatively infer that they might be, by considering long-term measurements of lighter and denser seawater export rates. First, Florindo-Lopez et al. (2020) analyze measurements of Arctic freshwater export west of Greenland spanning seven decades. While they identify significant decadal variability, they find no clear trend. Next, east of Greenland in Fram Strait, *ca.* two decades of freshwater fluxes show high variability with only a small (and recent) downwards trend (Karpouzoglou et al., 2022). Finally, the dense water export rate is known from the overflows across the Greenland–Iceland–Scotland Ridge. Østerhus et al. (2019) find no significant trend over more than two decades (and probably longer). Any significant change in Arctic Ocean water mass transformation rates should appear most clearly in the lighter water transports (once allowance is made for changes in meltwater runoff from the Greenland ice cap), because the overflows also include dense water formed in the Nordic Seas.

Regarding the future, sea ice is declining year-round in area, thickness and concentration (Cai et al., 2021; Stroeve & Notz, 2018), and is confidently forecast to disappear in summer during the present century (Jahn et al., 2024), while near-surface temperatures are increasing faster than the global mean, by nearly a factor of four (Rantanen et al., 2022). The ocean heat supply into the Arctic is increasing, both via the Barents Sea Opening (Wang et al., 2019) and Fram Strait (Wang et al., 2020). Oldenburg et al. (2024) find the Barents Sea ocean heat transport to be most important for future Arctic Ocean warming, while Barton et al. (2022) show that sea ice conditions in the Barents Sea may have crossed a threshold in the last decade. The most significant ongoing changes to the Arctic Ocean are described under the term "atlantification" by Polyakov et al. (2017). They define atlantification as the manifestation of a linked group of processes: the increased eastwards penetration into the Arctic Ocean, via volume transport and/or heat content, of the surface signature of Atlantic waters, the reduction in ice cover resulting in increased surface heat and moisture fluxes, and the increased depth of winter convection, bringing additional heat from Atlantic waters into the Arctic Surface water and transformation of the permanent halocline to a seasonal halocline. Part of the upper Arctic Ocean downstream from two gateways—Fram Strait and the Barents Sea Opening—is experiencing decreased stratification and increased mixing.

In the light of atlantification, future climate changes are likely to impact light and dense water formation, in terms of rates, locations and product water densities, and different regions may respond differently. We can speculate further, in the form of a chain of hypotheses, on the future evolution of the Arctic sea ice and ocean system, as the climate warms. Sea ice concentration, thickness and extent are expected to decrease through the present century. Sea ice reduction will increase the efficiency of atmosphere-to-ocean momentum transfer. One ocean response will be an increase in the strength of wind-driven turbulent mixing. However, measurements made by Lincoln et al. (2016) in ice-free Canadian Basin waters during a strong Arctic storm showed no penetration of energy associated with wind-driven near-inertial oscillations into Atlantic waters. It should also be noted that the combination of high latitude (low meridional gradient of the Coriolis parameter) and shallow mixed layers can

BROWN ET AL. 18 of 22

result in a six-fold reduction in near-inertial band energy in the Arctic Ocean as compared to similar mid-latitude scenarios (Guthrie & Morison, 2020): if the surface mixed layer is shoaling, then less energy will be transferred.

A second ocean response will entail increased momentum transfer accelerating the ocean circulation—in other words, the Arctic Ocean will "spin up"—a postulate expressed first by Giles et al. (2012), and subsequently by Rippeth et al. (2015) and Bacon (2023). Spin-up in turn will increase turbulence and mixing above its present widespread, weak baseline, so that Arctic currents and turbulence will tend toward open-ocean intensities elsewhere in the world ocean. Increased turbulence will increase the upwards flux of heat out of the sub-surface Atlantic Water toward the surface. These are all logical, physical consequences of sea ice reduction. At the same time, atmospheric warming will increase land ice melt (including from the Greenland and other smaller ice caps), and will also further accelerate the hydrological cycle, causing increased river runoff, and will probably increase sea surface temperatures.

If (more likely when) Arctic Ocean currents become faster and also more variable, and they are manifested around the boundary over the rough topography of the shelf edge, then the balance of physical processes that generate turbulent mixing will change. For instance, Rippeth et al. (2015) identify turbulent mixing "hotspots" allied with localized but strong tidal currents causing strong upwards heat fluxes. Subsequent studies (Baumann & Fer, 2023; Fer et al., 2020; Rippeth et al., 2017) associate these mixing hotspots with dissipation of unsteady lee wave processes, which are not presently included in model mixing parameterizations. Unsteady lee waves can form in response to any significant subinertial downslope flow, as shown by Schulz et al. (2021), who report enhanced mid-water TKE dissipation across the continental slope north of the Laptev Sea, a region of weak tidal flow. In this case, the downslope barotropic flow generating the unsteady lee wave is attributed to the passage of a continental shelf wave generated by a sub-Arctic storm. Danielson et al. (2020) and Schulz et al. (2021) show that the penetration of sub-Arctic-generated continental shelf waves is enhanced through reduced sea ice cover.

Unlike increases in wind-driven turbulent mixing, their significance of such processes lies in their potential to function at all depths, depending on the depths to which future increases in the strength of the inertial circulation may penetrate. Furthermore, a spun-up Arctic Ocean is expected to generate a much more eddy-rich environment (Li et al., 2024), so that property changes resulting from stronger mixing could be advected rapidly away from the boundary currents and into the ocean interior. The outstanding research questions, therefore, are: (a) where and by what mechanisms will Arctic Ocean turbulent mixing increase, (b) will the consequent increased upwards ocean heat flux reach the surface, and (c) if it reaches the surface, will it impact sea surface temperatures and/or sea ice thickness? How, therefore, will the "fight" between increased stratification and stronger turbulent mixing play out? Should it prove possible for a significant amount of sub-surface heat to reach the surface, the future Arctic Ocean will likely be qualitatively different from present predictions. A supplementary hypothesis arises: that atlantification represents (at least in part) the initialization of spin-up, whereby Atlantic waters are being "dragged" further into the Arctic Ocean. While conventional forced ice-ocean and coupled climate models can examine spin-up, new turbulence and mixing parameterizations are likely to be required to accommodate new processes.

Conflict of Interest

The authors declare no conflicts of interest relevant to this study.

Data Availability Statement

ERA-Interim reanalysis data (Dee et al., 2011) can be downloaded from https://cmr.earthdata.nasa.gov/search/concepts/C1214111003-SCIOPS. MERRA data (Rienecker et al., 2011) are available from https://disc.gsfc.nasa.gov/datasets?project=MERRA-2. The AOMIP river runoff dataset may be obtained from https://www2.whoi.edu/site/aomip/data/river-runoff-forcing-data/. The Arctic Ocean boundary data (Tsubouchi et al., 2012, 2018, 2021, 2024) can be downloaded from https://doi.pangaea.de/10.1594/PANGAEA.909966. The PHC climatology (Steele et al., 2001) can be downloaded from http://psc.apl.washington.edu/nonwp_projects/PHC/Climatology.html.

BROWN ET AL. 19 of 22

Acknowledgments

This paper is a contribution to UK NERC project CANARI (NE/W004984/1) and to project EPOC, EU Grant 101059547 and UKRI Grant 10038003. NJB acknowledges support from the SPITFIRE doctoral training partnership (UK Natural Environmental Research Council Grant NE/L002531/1). We are grateful to François Primeau and two anonymous reviewers for constructive feedback that helped to improve the manuscript.

References

- Bacon, S. (2023). Arctic sea ice, ocean and climate evolution. Science, 381(6661), 946–947. https://doi.org/10.1126/science.adj8469
- Bacon, S., Aksenov, Y., Fawcett, S., & Madec, G. (2015). Arctic mass, freshwater and heat fluxes: Methods and modelled seasonal variability. Philosophical Transactions of the Royal Society A, 373(2052), 20140169. https://doi.org/10.1098/rsta.2014.0169
- Bacon, S., Naveira Garabato, A. C., Aksenov, Y., Brown, N., & Tsubouchi, T. (2022). Arctic Ocean boundary exchanges: A review. *Ocean-ography*, 35, 94–102. https://doi.org/10.5670/oceanog.2022.133
- Barton, B., Lique, C., Lenn, Y.-D., & Talandier, C. (2022). An ice-ocean model study of the Mid-2000s regime change in the Barents Sea. *Journal of Geophysical Research*, 127(11), e2021JC018280. https://doi.org/10.1029/2021JC018280
- Baumann, T. M., & Fer, I. (2023). Trapped tidal currents generate freely propagating internal waves at the Arctic continental slope. *Scientific Reports*, 13(1), 14816. https://doi.org/10.1038/s41598-023-41870-3
- Bönisch, G., Blindheim, J., Bullister, J. L., Schlosser, P., & Wallace, D. W. R. (1997). Long-term trends of temperature, salinity, density, and transient tracers in the central Greenland Sea. *Journal of Geophysical Research*, 102(C8), 18553–18571. https://doi.org/10.1029/97JC00740
- Broecker, W. S. (1991). The great Ocean conveyor. *Oceanography*, 4(2), 79–89. https://doi.org/10.5670/oceanog.1991.07
- Cai, Q., Wang, J., Beletsky, D., Overland, J., Ikeda, M., & Wan, L. (2021). Accelerated decline of summer Arctic sea ice during 1850–2017 and the amplified Arctic warming during the recent decades. *Environmental Research Letters*, 16(3), 034015. https://doi.org/10.1088/1748-9326/ abdb5f
- Carmack, E., & Wassmann, P. (2006). Food webs and physical-biological coupling on pan-arctic shelves: Unifying concepts and comprehensive perspectives. *Progress in Oceanography*, 71(2–4), 446–477. https://doi.org/10.1016/j.pocean.2006.10.004
- Carmack, E. C. (2007). The alpha/beta ocean distinction: A perspective on freshwater fluxes, convection, nutrients and productivity in high-latitude seas. *Deep-Sea Research II*, 54(23–26), 2578–2598. https://doi.org/10.1016/j.dsr2.2007.08.018
- Cowtan, K., & Way, R. G. (2014). Coverage bias in the HadCRUT4 temperature series and its impact on recent temperature trends. *Quarterly Journal of the Royal Meteorological Society*, 140(683), 1935–1944. https://doi.org/10.1002/qj.2297
- Danielson, S. L., Hennon, T. D., Hedstrom, K. S., Pnyushkov, A. V., Polyakov, I. V., Carmack, E., et al. (2020). Oceanic routing of wind-sourced energy along the Arctic continental shelves. Frontiers in Marine Science, 7, 509. https://doi.org/10.3389/fmars.2020.00509
- Dee, D. P., Uppala, S. M., Simmons, A. J., Berrisford, P., Poli, P., Kobayashi, S., et al. (2011). The ERA-Interim reanalysis: Configuration and performance of the data assimilation system. *Quarterly Journal of the Royal Meteorological Society*, 137(656), 553–597. https://doi.org/10.1002/qj.828
- Eldevik, T., & Nilsen, J. E. O. (2013). The Arctic-Atlantic thermohaline circulation. *Journal of Climate*, 26(21), 8698–8705. https://doi.org/10.1175/JCLI-D-13-00305.1
- Fer, I., Koenig, Z., Kozlov, I., Ostrowski, M., Rippeth, T. P., Padman, L., et al. (2020). Tidally forced lee waves drive turbulent mixing along the Arctic Ocean margins. *Geophysical Research Letters*, 47(16), e2020GL088083. https://doi.org/10.1029/2020GL088083
- Florindo-Lopez, C., Bacon, S., Aksenov, Y., Chafik, L., Colbourne, E., & Holliday, N. P. (2020). Arctic Ocean and Hudson Bay freshwater exports: New estimates from 7 decades of hydrographic surveys on the Labrador shelf. *Journal of Climate*, 33(20), 8849–8868. https://doi.org/ 10.1175/JCLI-D-19-0083.1
- Giles, K. A., Laxon, S. W., Ridout, A. L., Wingham, D. J., & Bacon, S. (2012). Western Arctic Ocean freshwater storage increased by wind-driven spin-up of the Beaufort Gyre. *Nature Geoscience*, 5(3), 194–197. https://doi.org/10.1038/ngeo1379
- Guthrie, J. D., & Morison, J. H. (2020). Not just sea ice: Other factors important to near-inertial wave generation in the Arctic Ocean. *Geophysical Research Letters*, 48(3), e2020GL090508. https://doi.org/10.1029/2020GL090508
- Haine, T. W. N. (2021). A conceptual model of polar overturning circulations. *Journal of Physical Oceanography*, 51(3), 727–744. https://doi.org/10.1175/JPO-D-20-0139.1
- IMBIE Team. (2020). Mass balance of the Greenland Ice Sheet from 1992 to 2018. Nature, 579(7798), 233–239. https://doi.org/10.1038/s41586-019-1855-2
- Isachsen, P. E., Mauritzen, C., & Svendsen, H. (2007). Dense water formation in the Nordic Seas diagnosed from sea surface buoyancy fluxes. Deep-Sea Research 1, 54(1), 22–41. https://doi.org/10.1016/j.dsr.2006.09.008
- Jahn, A., Holland, M. M., & Kay, J. E. (2024). Projections of an ice-free Arctic Ocean. *Nature Reviews Earth & Environment*, 5(3), 164–176. https://doi.org/10.1038/s43017-023-00515-9
- Jullion, L., Heywood, K. J., Naveira Garabato, A. C., & Stevens, D. P. (2010). Circulation and water mass modification in the Brazil-Malvinas confluence. *Journal of Physical Oceanography*, 40(5), 845–864. https://doi.org/10.1175/2009JPO4174.1
- Karpouzoglou, T., de Steur, L., Smedsrud, L. H., & Sumata, H. (2022). Observed changes in the Arctic freshwater outflow in Fram Strait. *Journal of Geophysical Research*, 127(3), e2021JC018122. https://doi.org/10.1029/2021JC018122
- Karstensen, J., Schlosser, P., Wallace, D. W. R., Bullister, J. L., & Blindheim, J. (2005). Water mass transformation in the Greenland Sea during the 1990s. *Journal of Geophysical Research*, 110(C7), C07022. https://doi.org/10.1029/2004JC002510
- Kipp, L. E., Kadko, D. C., Pickart, R. S., Henderson, P. B., Moore, W. S., & Charette, M. A. (2019). Shelf-basin interactions and water mass residence times in the Western Arctic Ocean: Insights provided by radium isotopes. *Journal of Geophysical Research*, 124(5), 3279–3297. https://doi.org/10.1029/2019JC014988
- Lambert, E., Eldevik, T., & Haugan, P. M. (2016). How northern freshwater input can stabilise thermohaline circulation. *Tellus*, 68(1), 31051. https://doi.org/10.3402/tellusa.v68.31051
- Large, W. G., & Nurser, A. J. G. (2001). Ocean surface water mass transformation. In G. Siedler, J. Church, & W. J. Gould (Eds.), Ocean circulation and climate, international geophysics (Vol. 77, pp. 317–336). Academic Press. https://doi.org/10.1016/S0074-6142(01)80126-1
- Lenn, Y.-D., Fer, I., Timmermans, M.-L., & MacKinnon, J. A. (2022). Chapter 11 Ocean mixing. In M. Meredith & A. C. Naveira Garabato (Eds.), Mixing in the Arctic Ocean (pp. 275–299). Elsevier. https://doi.org/10.1016/B978-0-12-821512-8.00018-9
- Li, X., Wang, Q., Danilov, S., Koldunov, N., Liu, C., Müller, V., et al. (2024). Eddy activity in the Arctic Ocean projected to surge in a warming world. *Nature Climate Change*, 14(2), 156–162. https://doi.org/10.1038/s41558-023-01908-w
- Lincoln, B. J., Rippeth, T. P., Lenn, Y.-D., Timmermans, M. L., Williams, W. J., & Bacon, S. (2016). Wind-driven mixing at intermediate depths in an ice-free Arctic Ocean. *Geophysical Research Letters*, 43(18), 9749–9756. https://doi.org/10.1002/2016GL070454
- Lindsay, R., Wensnahan, M., Schweiger, A., & Zhang, J. (2014). Evaluation of seven different atmospheric reanalysis products in the Arctic. Journal of Climate, 27(7), 2588–2606. https://doi.org/10.1175/JCLI-D-13-00014.1
- Lique, C., & Steele, M. (2012). Where can we find a seasonal cycle of the Atlantic water temperature within the Arctic Basin? *Journal of Geophysical Research*, 117(C3), C03026. https://doi.org/10.1029/2011JC007612
- Lobb, J., Weaver, A. J., Carmack, E. C., & Ingram, R. G. (2003). Structure and mixing across and Arctic/Atlantic front in northern Baffin Bay. Geophysical Research Letters, 30, 1833. https://doi.org/10.1029/2003GL017755

BROWN ET AL. 20 of 22

oceanog.2022.116

2025, 6, Down

ibrary on [18/11/2025]. See the Term:

- Lozier, M. S., Bacon, S., Bower, A. S., Cunningham, S. A., de Jong, M. F., de Steur, L., et al. (2017). Overturning in the subpolar North Atlantic program. *Bulletin America Meteorology Social*, 98, 737–752. https://doi.org/10.1175/BAMS-D-16-0057.1
- Lozier, M. S., Li, F., Bacon, S., Bahr, F., Bower, A. S., Cunningham, S. A., et al. (2019). A sea change in our view of the subpolar North Atlantic. Science, 363(6426), 516–521. https://doi.org/10.1126/science.aau6592
- Mayer, M., Tietsche, S., Haimberger, L., Tsubouchi, T., Mayer, J., & Zuo, H. (2019). An improved estimate of the coupled Arctic energy budget. Journal of Climate, 32(22), 7915–7934. https://doi.org/10.1175/JCLI-D-19-0233.1
- Naveira Garabato, A. C., Oliver, K. I. C., Watson, A. J., & Messias, M.-J. (2004). Turbulent diapycnal mixing in the Nordic Seas. *Journal of Geophysical Research*, 109(C12), C12010. https://doi.org/10.1029/2004JC002411
- Oldenburg, D., Kwon, Y.-O., Frankignoul, C., Danabasoglou, G., Yeager, S., & Kim, W. H. (2024). The respective roles of ocean heat transport and surface fluxes in driving Arctic Ocean warming and sea ice decline. *Journal of Climate*, 37(4), 1431–1448. https://doi.org/10.1175/JCLI-D-
- Østerhus, S., Woodgate, R., Valdimarsson, H., Turrell, B., de Steur, L., Quadfasel, D., et al. (2019). Arctic Mediterranean exchanges: A consistent volume budget and trends in transports from two decades of observations. *Ocean Science*, 15(2), 379–399. https://doi.org/10.5194/os-15-379-2019
- Padman, L. (1995). Small-scale physical processes in the Arctic Ocean. Chapter 3. In W. O. Smith Jr. & J. M. Grebmeier (Eds.), Arctic oceanography: Marginal ice zones and continental shelves, coastal and estuarine studies (Vol. 49, pp. 97–129). American Geophysical Union. https://doi.org/10.1029/CE049p0097
- Pemberton, P., Nilsson, J., Hieronymus, M., & Meier, H. E. M. (2015). Arctic Ocean water mass transformation in S-T coordinates. *Journal of Physical Oceanography*, 45(4), 1025–1050. https://doi.org/10.1175/JPO-D-14-0197.1
- Polyakov, I. V., Pnyushkov, A. V., Alkire, M. B., Ashik, I. M., Baumann, T. M., Carmack, E. C., et al. (2017). Greater role for Atlantic inflows on sea-ice loss in the Eurasian Basin of the Arctic Ocean. Science, 356(6335), 285–291. https://doi.org/10.1126/science.aai8204
- Prange, M., & Lohmann, G. (2004). Variable freshwater input to the Arctic Ocean during the Holocene: Implications for large-scale ocean-sea ice dynamics as simulated by a circulation model. In H. Fischer (Ed.), *The climate in historical times, GKSS school of environmental research* (pp. 319–335). Springer. https://doi.org/10.1007/978-3-662-10313-5_18
- Rahmstorf, S. (2002). Ocean circulation and climate during the last 120,000 years. *Nature*, 419(6903), 207–214. https://doi.org/10.1038/nature01090
- Rantanen, M., Karpechko, A. Y., Lipponen, A., Nordling, K., Hyvärinen, O., Ruosteenoja, K., et al. (2022). The Arctic has warmed nearly four times faster than the globe since 1979. *Nature Communications Earth and Environment*, 3(1), 168. https://doi.org/10.1038/s43247-022-00498-3
- Rienecker, M. M., Suarez, M. J., Gelaro, R., Todling, R., Bacmeister, J., Liu, E., et al. (2011). MERRA: NASA's modern-era retrospective analysis for research and applications. *Journal of Climate*, 24(14), 3624–3648. https://doi.org/10.1175/JCLI-D-11-00015.1
- Ripperth, T. P., & Fine, E. C. (2022). Turbulent mixing in a changing Arctic Ocean. *Oceanography*, 35, 42–51. https://doi.org/10.5670/oceanog. 2022.103
- Rippeth, T., Lincoln, B. J., Lenn, Y.-D., Green, J. A. M., Sundfjord, A., & Bacon, S. (2015). Tide-mediated warming of the Arctic halocline by Atlantic water heat fluxes over rough topography. *Nature Geoscience*, 8(3), 191–194. https://doi.org/10.1038/NGEO2350
- Rippeth, T. P., Vlasenko, V., Stashchuk, N., Scannell, B. D., Green, J. A. M., Lincoln, B. J., & Bacon, S. (2017). Tidal conversion and mixing poleward of the critical latitude (an Arctic case study). *Geophysical Research Letters*, 44(24), 12-349. https://doi.org/10.1002/2017GL075310 Rudels, B. (2010). Constraints on exchanges in the Arctic Mediterranean—Do they exist and can they be of use? *Tellus*, 62A(2), 109–122. https://
- doi.org/10.1111/j.1600-0870.2009.00425.x
 Rudels, B., & Carmack, E. C. (2022). Arctic Ocean water mass structure and circulation. *Oceanography*, 35, 52–65. https://doi.org/10.5670/
- Schulz, K., Büttner, S., Rogge, A., Janout, M., Hölemann, J., & Rippeth, T. P. (2021). Turbulent mixing and the formation of an intermediate nepheloid layer above the Siberian continental shelf break. *Geophysical Research Letters*, 48, e2021GL092988. https://doi.org/10.1029/2021GL092988
- Serreze, M. C., Barrett, A. P., Slater, A. G., Steele, M., Zhang, J., & Trenberth, K. E. (2007). The large-scale energy budget of the Arctic. *Journal of Geophysical Research*, 112(D11), D11122. https://doi.org/10.1029/2006JD008230
- Shiklomanov, A., Déry, S., Tretiakov, M., Yang, D., Magritsky, D., Georgiadi, A., & Tang, W. (2021). River freshwater flux into the Arctic Ocean. Chapter 24. In D. Yang & D. L. Kane (Eds.), Arctic hydrology, Permafrost and ecosystems (pp. 703–738). Springer Nature. https://doi.org/10.1007/978-3-030-50930-9_24
- Steele, M., Morley, R., & Ermold, W. (2001). PHC: A global ocean hydrography with a high-quality Arctic Ocean. *Journal of Climate*, 14(9), 2079–2087. https://doi.org/10.1175/1520-0442(2001)014<2079:PAGOHW>2.0.CO;2
- Stigebrandt, A. (1981). A model for the thickness and salinity of the upper layer in the Arctic Ocean and the relationship between the ice thickness and some external parameters. *Journal of Physical Oceanography*, 11(10), 1407–1422. https://doi.org/10.1175/1520-0485(1981)011<1407: AMFTTA>2.0.CO;2
- Stroeve, J., & Notz, D. (2018). Changing state of Arctic sea ice across all seasons. Environmental Research Letters, 13(10), 103001. https://doi.org/10.1088/1748-9326/aade56
- Tsubouchi, T., Bacon, S., Aksenov, Y., Naveira Garabato, A. C., Beszczynska-Möller, A., Hansen, E., et al. (2018). The Arctic Ocean seasonal cycles of heat and freshwater fluxes: Observation-based inverse estimates. *Journal of Physical Oceanography*, 48(9), 2029–2055. https://doi.org/10.1175/JPO-D-17-0239.1
- Tsubouchi, T., Bacon, S., Naveira Garabato, A. C., Aksenov, Y., Laxon, S. W., Fahrbach, E., et al. (2012). The Arctic Ocean in summer: A quasi-synoptic inverse estimate of boundary fluxes and water mass transformation. *Journal of Geophysical Research*, 117(C1), C01024. https://doi.org/10.1029/2011JC007174
- Tsubouchi, T., Våge, K., Hansen, B., Larsen, K. M. H., Østerhus, S., Johnson, C., et al. (2021). Increased ocean heat transport into the Nordic Seas and Arctic Ocean over the period 1993–2016. *Nature Climate Change*, 11(1), 21–26. https://doi.org/10.1038/s41558-020-00941-3
- Tsubouchi, T., von Appen, W.-J., Kanzow, T., & de Steur, L. (2024). Temporal variability of the overturning circulation in the Arctic Ocean and the associated heat and freshwater transports during 2004–10. *Journal of Physical Oceanography*, 54, 81–94. https://doi.org/10.1175/JPO-D-23-0056.1
- Walin, G. (1982). On the relationship between sea surface heat flow and thermal circulation in the ocean. *Tellus*, 34(2), 187–195. https://doi.org/10.1111/j.2153-3490.1982.tb01806.x
- Wang, Q., Wang, X., Wekerle, C., Danilov, S., Jung, T., Koldunov, N., N., et al. (2019). Ocean heat transport into the Barents Sea: Distinct controls on the upward trend and interannual variability. Geophysical Research Letters, 46(22), 13180–13190. https://doi.org/10.1029/2019GL083837

BROWN ET AL. 21 of 22



- Wang, Q., Wekerle, C., Wang, X., Danilov, S., Koldunov, N., Sein, D., D., et al. (2020). Intensification of the Atlantic Water supply to the Arctic Ocean through Fram Strait induced by Arctic sea ice decline. *Geophysical Research Letters*, 47(3), e2019GL086682. https://doi.org/10.1029/2019GL086682
- Wefing, A.-M., Casacuberta, N., Christl, M., Gruber, N., & Smith, J. N. (2021). Circulation timescales of Atlantic Water in the Arctic Ocean determined from anthropogenic radionuclides. *Ocean Science*, 17(1), 111–129. https://doi.org/10.5194/os-17-111-2021
- Weijer, W., Haine, T. W. N., Siddiqui, A. H., Cheng, W., Veneziani, M., & Kurtakoti, P. (2022). Interactions between the Arctic Mediterranean and the Atlantic meridional overturning circulation. *Oceanography*, 35, 118–127. https://doi.org/10.5670/oceanog.2022.130
- Wilson, C., Aksenov, Y., Rynders, S., Kelly, S. J., Krumpen, T., & Coward, A. C. (2021). Significant variability of structure and predictability of Arctic Ocean surface pathways affects basinwide connectivity. *Communications Earth & Environment*, 2(1), 164. https://doi.org/10.1038/s43247-021-00237-0
- Zhang, R., & Thomas, M. (2021). Horizontal circulation across density surfaces contributes substantially to the long-term mean northern Atlantic Meridional Overturning Circulation. *Nature Commun. Earth & Environment*, 2(1), 112. https://doi.org/10.1038/s43247-021-00182-y

References From the Supporting Information

- Gregg, M., D'Asaro, E., Riley, J., & Kunze, E. (2018). Mixing efficiency in the ocean. Annual Review of Marine Science, 10(1), 443–473. https://doi.org/10.1146/annurev-marine-121916-063643
- Vic, C., Naveira Garabato, A. C., Green, J. A. M., Waterhouse, A. F., Zhao, Z., Melet, A., et al. (2019). Deep-ocean mixing driven by small-scale internal tides. *Nature Communications*, 10(1), 2099. https://doi.org/10.1038/s41467-019-10149-5

BROWN ET AL. 22 of 22